Tampere University

Fernando Galaz Prieto

MC-tES in Zeffiro Interface: Sparse Optimized and Regularized Stimulus

Faculty of Information Technology and Communication Sciences (ITC)
Master's thesis
December 2020

Abstract

Fernando Galaz Prieto: MC-tES in Zeffiro Interface: Sparse Optimized and Regularized Stimulus
Master's thesis
Tampere University
Master's Degree Programme in Information Technology
December 2020

This thesis aims to describe the mathematical methodology of multi-channel transcranial electrical stimulation (MC-tES) and its computational implementation in the open Matlab-based Zeffiro Interface (ZI) toolbox. The goal is to extend the current solver capabilities of ZI, and by using the solver implementation, among other things, to enlighten the process of finding a focal optimized, and preferably sparse, current pattern, as well as to provide the necessary codes for further software development. The present implementation covers both forward and inverse MC-tES solver. The former inherits for ZI's finite element method based forward solver for electroencephalography. Here the mathematical framework of this solver is described and its connection to MC-tES explained. The application of the complete electrode model boundary conditions ensures the high accuracy of the model at the vicinity of the current-injecting electrodes. The inverse problem is approached via ℓ_1-regularized optimization and the dual-simplex linear programming algorithm. The performance of the implementation is evaluated in numerical experiments in which the volume current density caused by the stimulus is steered using a synthetic 10 nAm source with a reference extent of 253 mm^3 as a target. A rough initial range for the regularization and tolerance parameter is found with somatosensory, visual and auditory cortex as the reference target areas, using a realistic multi-layered head model discretized with 1 mm accuracy.

Keywords: Multi-Channel Transcranial Electrical Stimulation (MC-tES), Electroencephalography (EEG), Forward and Inverse Problem, Finite Element Method (FEM), Optimization

Contents

1 Introduction

This thesis project aims to extend the capabilities of Finite Element Method (FEM)-based forward and inverse methodology in the mathematical modeling the electromagnetic fields generated by and targeting the human brain in the detection and manipulation of brain activity. Following up from previous electroencephalography (EEG) and magnetoencephalography (MEG) studies and implementations (Mainalainen et al. 2019), the intention is to implement a combination of mathematical statistics and principles of optimization for enhancing focality of the stimulus within the brain and sparsity of the corresponded current pattern, i.e., reducing the number of required electrodes utilized during a EEG/MC-tES session. The main approach of the study is implemented in MATLAB, MathWorks[1].

Zeffiro Interface (ZI)[2] is an open-source brain imaging toolbox designed to provide a multi-modality platform for FEM-based, graphic processing unit (GPU)-accelerated forward and inverse computations (He et al. 2019). As part of this thesis, a script was generated serving as an update to the current version. The goal is to extend forward solvers into including multi-channel transcranial electrical stimulation (MC-tES), a non-invasive brain stimulation (NIBS) technique, in addition to EEG and MEG solvers that ZI already presents. It also serves as the initial contribution for preparing the MC-tES workbench in ZI and provides direction for further development of forward and inverse modeling software.

The contents of this thesis are to provide sufficient information to understand the basis of the activities executed on this project: health informatics in the form of biosignal analysis, mathematics in the form of statistics and optimization, and information technologies in the form of code development. Each of the chapters presented in this thesis constitutes a timid introduction to their respective fields, the goal and focus being in the mathematical methodology and its application to MC-tES.

After describing the principles of MC-tES, the mathematical forward model and it discretization, that is the lead field matrix of MC-tES, is briefly reviewed. Subsequently, the mathematical optimization on ℓ_1 norm minimization and regularization, thereby focal and sparse distribution (Kaipio and Somersalo 2006) is described. To examine the performance of the present implementation, the combination of forward and inverse solvers is applied to find a focal stimulus pattern concentrated in a given target area of the brain. A realistic multi-layer head model discretized with 1 millimeter (mm) resolution is applied in this process, and a dipolar source

[1] `https://www.mathworks.com/`

[2] `https://github.com/sampsapursiainen/zeffiro_interface`

current placed in the cerebral cortex is used as targeted brain activity with somatosensory, visual and auditory brain areas as reference locations. To enhance the sparsity and quality of the elicited current pattern injected by the electrodes, we consider both thresholding and re-optimization of said thresholded pattern, as potential approaches.

This thesis is organized as follows: Neurological background is explained in Chapter 2; Transcranial Electrical Stimulation, application and methods, are described in Chapter 3. Furthermore, mathematical background that encompasses the forward model is described in Chapter 4. Optimization procedure, including linear programming, is described in Chapter 5. Results are presented in Chapter 6. Lastly, conclusions are presented in Chapter 8.

2 Neurological Background

This chapter provides a general overview of the human brain including their structure, neural circuitry and cognitive basics. Profound anatomical knowledge is not required as required information is kept to a minimum. On this chapter, the corresponding electrical activity is explained in section 2.1 and, thereby, understanding the functionality of EEG/MC-tES in section 2.2.

2.1 The brain and it functionality

The human brain is a sophisticated array of sensory receptors responsible for the control and coordination of all actions and reactions over the human behaviour and all their physiological functionalities (Kandel et al. 2012). It consists of a large number of specialized parts serving a variety of cognitive processes that allows us to enact any kind of activity, including information processing, reflexes, management of biostasis, and emotion based on hormonal and neurotransmitters reactions such as dopamine, serotonin, adrenaline. The brain is protected by the skull, meninges layers, and suspended in cerebrospinal fluid (CSF) (Fig. 2.1). Further information on central nervous system (CNS), which includes the brain, is provided in 2.1.1, their conductive components on section 2.1.2, and the biochemical signaling processing is explained on section 2.1.3.

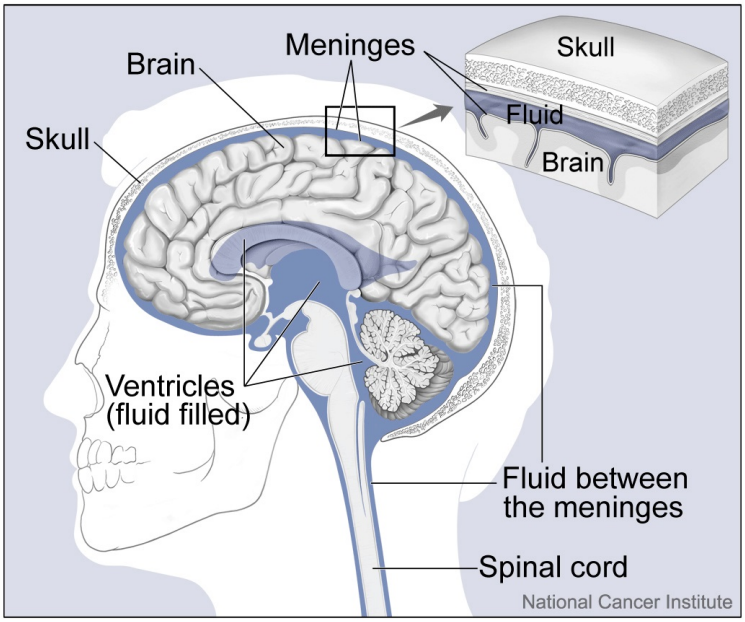

Figure 2.1 *The brain and nearby structures (including the skull, meninges, ventricles and spinal cord). An enlarged inset shows the skull, fluid, and brain.*[1]

2.1.1 Central Nervous System (CNS)

The central nervous system (CNS) consists of seven main parts: the spinal cord, medulla oblongata, pons, cerebellum, midbrain, diencephalon and cerebrum. With the exception of the spinal cord, the remaining six parts together form the brain. The brain is commonly divided into three regions: the *forebrain*, which constitutes the cerebrum and diencephalon; the *midbrain*, which involves medulla oblongata, pons, and cerebellum; and the *hindbrain*, which refer to the same structures previously mentioned in the midbrain with exception of the cerebellum. Brief explanation of the parts of the CNS is presented as following (Fig. 2.2):

1. The *spinal cord* is the most caudal part of the CNS and is responsible for receiving, processing and controlling information from the skin, muscles and joints of the limbs and trunk. The *brain stem*, which consists of medulla oblongata, pons and midbrain, is responsible for information detection from the skin and muscles in the head, controlling musculature of the face, neck and eyes and processing information such as hearing, balance and taste. It serves as the intermediary between the brain and the spinal cord and it regulates arousal and awareness levels based on the stimulus perceived by the reticular formation.
2. The *medulla oblongata* is rostral to the spinal cord and is responsible for vital autonomic basic functions such as controlling respiration, heart rate, regulation of blood pressure, and reflexes as in coughing, swallowing and vomiting.
3. The *pons* is rostral to the medulla oblongata and is in charge of conveying movement information to the cerebrum from the cerebral hemispheres.
4. The *cerebellum* is located directly behind the medulla oblongata and the pons and is responsible for modulating the necessary amount of force and distance of motor movements. It is also involved in the learning of new motor skills.
5. The *midbrain* is rostral to the pons and controls sensor and motor of the eyes and the coordination of audio-visual reflexes.
6. The *diencephalon* is rostral to the midbrain and is divided into two structures: *thalamus* and *hypothalamus*. The former acts as an information processor while the latter performs regulation of autonomic, endocrine, and visceral functions such like thermal regulation, body water, sleep cycle.
7. The *cerebrum* is the main structure of the CNS and is compromised of two hemispheres. Together they forms the largest part of the brain. Each of the

[1](`https://www.flickr.com/photos/132318516@N08/26276988755`) by Alan Hoofring (Illustrator), National Cancer Institute, National Institutes of Health, 6 April 2016, Public Domain.

hemispheres consist of two structures: an outer layer of folded neuronal tissue, known as *cerebral cortex* surrounded by grey matter, and a three deep-lying structure: the *basal ganglia*, which regulates motor performance, the *hippocampus*, involved in memory management, and *amygdaloid nuclei*, responsible for autonomic and endocrine responses of emotional states. Each one of the hemispheres are divided into four lobes: frontal lobe, parietal lobe, temporal lobe, and occipital lobe.

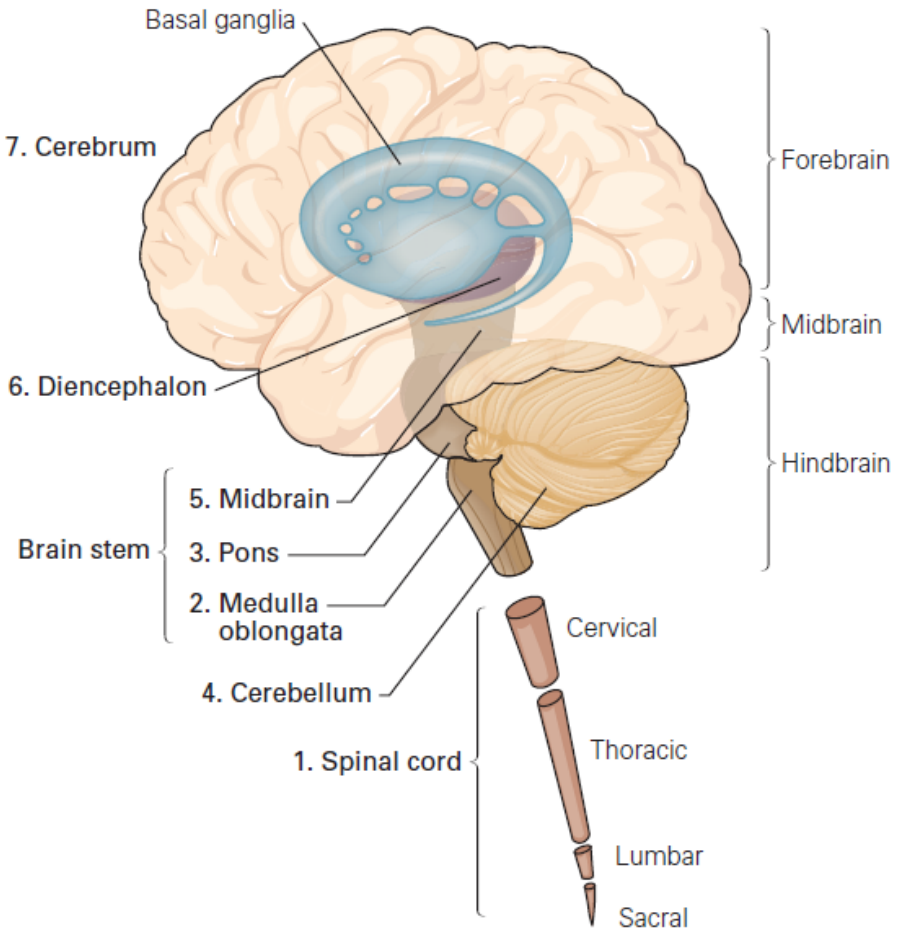

Figure 2.2 *The central nervous system divided into seven main parts: (1) Spinal cord and the four major parts: Cervical, Thoracic, Lumbar and Sacral. (2) Medulla oblongata. (3) Pons. (4) Cerebellum (5) Midbrain (6) Diencephalon, and (7) Cerebrum. The Basal ganglia displayed at the center (Kandel et al. 2012).*

2.1.2 Neural Circuitry in the Brain

The entire CNS requires a method to communicate with every part of the system. This is performed via a complex network of *neurons* within the nervous tissue which is dedicated to carry information through an electro-chemical procedure. This section concisely describes how this process is done.

The structure of a typical neuron consists of four specific regions: cell body, axons, dendrites and pre-synaptic terminals (Fig. 2.3). The cell body, or *soma*, is the powerhouse of the nerve cell. It contains the nucleus, where genetic information is located, and the endoplasmic reticulum, a nucleus-extension where the protein of the cell is synthesized. The morphology of the cell body gives rise to axon and dendrites. The *axon* is a long, singular tube, of range varying between 0.1mm to 2m (Kandel et al. 2012), encased by multiple tubings knowns as *Myelin sheaths* and separated by nodes of Ranvier. Axons are responsible for delivering information to the other nerve cells through electrical signals known as *action potentials* (described on 2.1.3). The *dendrites*, which are tree branch-shape terminals of approximately 2mm (Sörnmo and Laguna 2005), are responsible for receiving any incoming signal from the axons through the neuronal junction that connects these two neurons. This junction is called *synapse*.

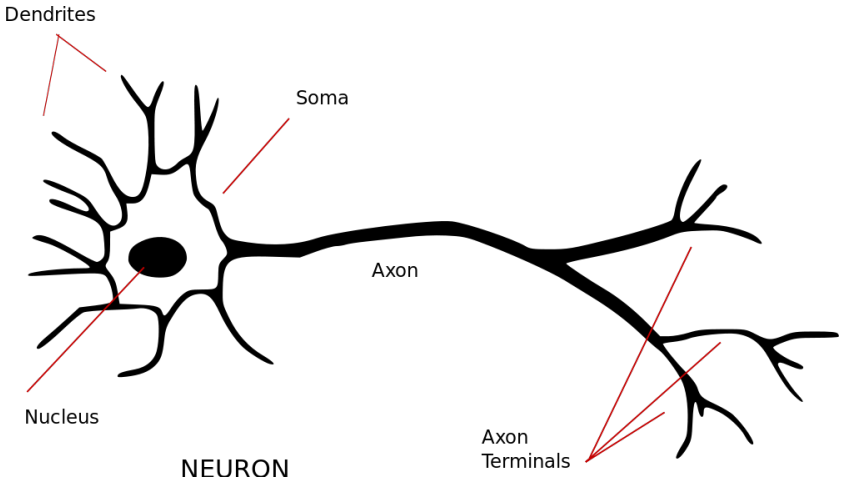

Figure 2.3 *Illustration of a typical nerve cell.*[2]

Aside from neurons being the most influencing type of cell among the neural tissue, there are other non-neuronal cells that can be found within the CNS that do not produce their own electrical impulses: *glial cells* (also glia or neuroglia). The glial cells behave as a type of supportive cell for the neurons. Originally, they were believed to just provide structural support, hence the name, "glía" derived from the ancient Greek word which literally means "glue" in English (Jäkel and Dimou 2017). This type of cell are what makes up the white matter within the brain. The population of this cell can be further subdivided into four groups: astrocytes, microglia, NG2-glia, and oligodendrocytes. The latter type of cell is the one responsible for laying the myelin sheaths wrapping around the axons, facilitating the current flow across the axon.

[2] `https://commons.wikimedia.org/wiki/File:Neurone.png`, by Looxix, 19 October 2003, CC BY-SA 3.0.

The entire neuronal tissue in the brain is spread among other structures, including blood vessels and, most importantly, the ventricle system which consists of a system of compartments within the CNS. Broadly speaking, the ventricle system provides an aqueduct system for the distribution of CSF providing basic immunological protection and mechanical fluid-based suspension between brain and skull. Additionally, the fluid provides the autoregulation of cerebral blood flow maintaining constant blood flow.

2.1.3 Action Potential and Post-Synaptic Potentials

An *action potential* (AP) is the change in membrane potential that propagate along the surface of excitable cells, characterized by being "all-or-nothing", i.e. they have a threshold for arousal and a stereotyped duration; immediately after one AP, the excitable cell has a refractory period during which makes it difficult to trigger a secondary trigger right after the initial one. They are the result of changes in membrane permeability due to the activity of channels, or proteins embedded in the lipid bi-layer membrane that facilitate the passive movement of specific ions in favor of their electro-chemical gradients.

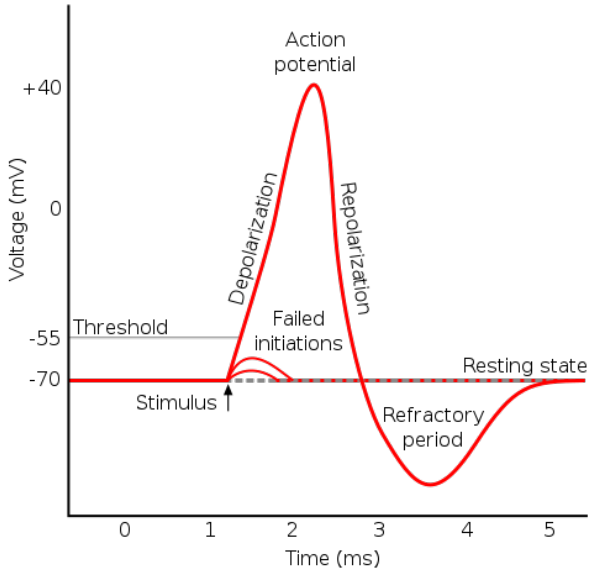

Figure 2.4 *Representation of an single action potential and all their electrical properties.*

Synapses are known as the communication between a neuron cell and a target cell, whether can be a muscle, a gland or another neuron. In this case, the sending cell is known as *pre-synaptic* while the receiving cell as *post-synaptic*. Because of its structure, an axon is capable of communicating with multiple post-synaptic cells. Refer to Fig. 2.5. Inside each axon terminal are multiple *synaptic vesicles*, and membranes which are filled with neurotransmitter molecules.

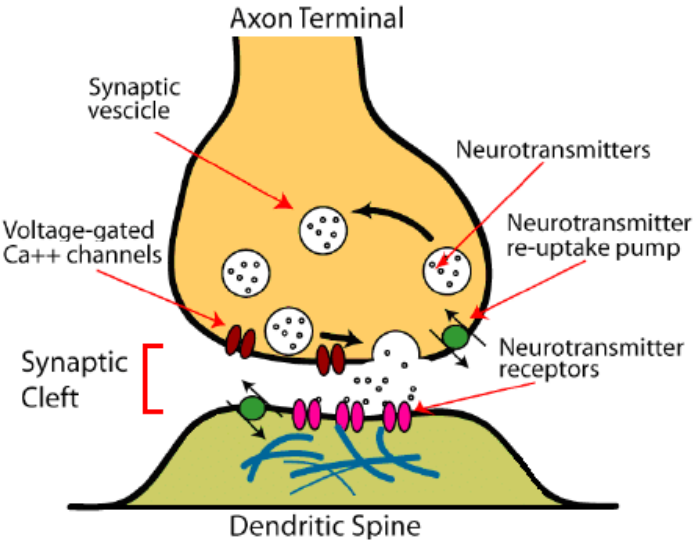

Figure 2.5 *Formation of post-synaptic potentials.*[3]

Whenever an AP triggers and arrives at the axon terminals, it activates the voltage-gated calcium channels in the membrane allowing an income of Ca^{2+} inside the cell. This increasing level of Ca^2+ allows the synaptic vesicle to temporally fuse with the axon membrane, creating an opening and releasing their neurotransmitters to the *synaptic cleft*, the gap that separates the connection between two cells. While the inside of the target cell is dominated by potassium-ions ($K+$), the synaptic cleft containing more sodium ($Na+$) and chloride ($Cl-$) leads to a negative concentration gradient causing a difference in electric potential between the interior of the cell and the outside. The released neurotransmitters, which are propagating across the synaptic cleft, binds to the target cell, causing the ionic channels of the membrane to open or close, causing a dramatic change of electric potential inside of the cell: If the membrane opens and $Na+$ flows in, the potential inside of the neuron increases. If enough neurotransmitters binds, neuron's potential can reach firing threshold levels. This is known as depolarizing potential, or *excitatory post-synaptic potential* (EPSP). In contrast, if $Cl-$ instead flows into the cell, then the potential decreases reducing the neuron's ability to trigger an action potential. This is known as hyperpolarizating potential, or *inhibitory post-synaptic potential* (IPSP). Both EPSP and IPSP (also known as *graded potentials*) are transient changes in the membrane potential. It is important to mention that a singular PSP on it own cannot provide sufficient potential to trigger the next action potential unless the summation of voltage from multiple PSP instances can reach the threshold level (Fig. 2.6)

[3] `https://commons.wikimedia.org/wiki/File:Sinapsis.png` (Translated), by DaDez, 13 February 2006, CC BY-SA 3.0.

[4] `https://med.libretexts.org/@go/page/7596?pdf`, by LibreTexts, 18 December 2020, CC BY-SA 3.0.

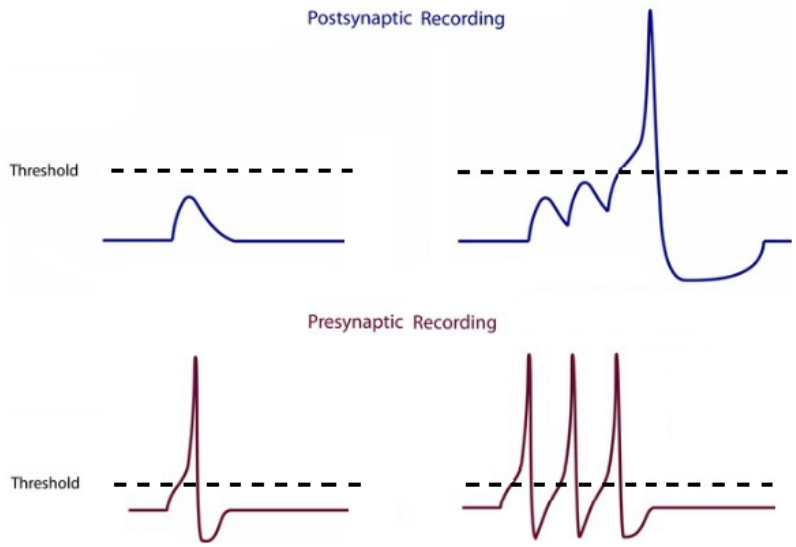

Figure 2.6 *Comparison between graded potential (blue) and action potential (red). Graded potentials are temporary changes in the membrane potential that do not yield enough strength to depolarize above the threshold level. This condition can be met if the summation of postsynaptic potentials across the axon passes the threshold level.*[4]

2.2 Understanding Electroencephalogram (EEG)

Electroencephalography (EEG) is defined as the recording of brain electrical activity, obtained from the scalp by placing surface electrodes (Schomer and Silva 2012). EEG is useful for studying neuronal activity, understating cognitive behaviour and discover network communication with neurons via electrical impulses. During interpretation of EEG results its necessary to have knowledge of the normal activity in the different ages and clinical states of the patient, as well as the identification of artifacts, technical problems and marginal patterns, in order to avoid interpretation errors or overlooking findings that could be abnormal.

The described processes in section 2.1.3 offer electric potentials in two distinctive forms which can be detected in the brain. While AP are short bursts of current change in the axons followed by a repolarization phase, PSP have the opposite properties, having a weaker burst instead but taking longer time to diminish (Hämäläinen et al. 1993). Although AP are much stronger than PSPs in terms of voltage, it is assumed that the measured current activity by the EEG arises mainly from the PSPs.

3 Transcranial Electrical Stimulation (tES)

Transcranial Electrical Stimulation (tES) is a form of NIBS method for stimulating the neuronal activity and treating psychiatric disorders and studying neuronal behavior under the influence of continuous, low-intensity current applied to a specific region of interest (ROI) of the brain. The current dose applied is defined, but not limited, by the electrode parameters (total number of electrodes, positioning, shape, and composition), stimulation waveform (amplitude, pulse shape, amplitude, width, polarity) and number of stimulation sessions including the time interval between each sessions (Peterchev et al. 2012); generally traveling through the soft tissue and skull (Vöröslakos et al. 2018), should be high enough to penetrate the scalp, able to increase or decrease intrinsic neuronal excitability (Miniussi et al. 2013), while low enough to prevent severe significant adverse effects during and after stimulation session.

Numerous experiments had resorted these electrostimulating methods to study various neuropsychiatric disorders and brain illnesses including stroke conditions (Fregni et al. 2005b; Lindenberg et al. 2010), epilepsy syndromes (Fregni et al. 2006a), Parkinson's disease (Boggio et al. 2006; Benninger et al. 2010; Fregni et al. 2005a; Fregni et al. 2006c), major depression disorder (Boggio et al. 2007; Fregni et al. 2006d; Nitsche et al. 2009), tinnitus (ringing in ear) (Fregni et al. 2006b), migraine (Antal et al. 2003), and alcoholism (Boggio et al. 2008).

3.1 Application

To apply tES, a set of at least two or more metal or conductive-rubber electrodes with saline-soaked sponges must be attached to the scalp of the head model (DaSilva et al. 2011; Ukueberuwa and Wassermann 2010) where the underneath lobes of the brain to be stimulated area can be identified. The shape and size of the saline-soaked sponges attached to the terminals must be designed to uniformly distribute the current over the stimulation area for preventing an eletrical concentration on the skin-sponge interface, reducing skin irritability generated by these methods (Furubayashi et al. 2008). Deployment of these electrodes can follow directly from International EEG 10-10 or 10-20 system (see Fig. 3.1); the ROI of the subject is determined by measuring distances between inion to the nasion, and from left pre-auricular to the right pre-auricular (Klem 1999).

The distance between the electrodes applied across the scalp and the electric generator (or an voltage-fixed battery) will function as a closed-circuitry where the stimulation current (in mA) travels for a fixed amount of time (measured in minutes)

from the positive lead (also known as *anode or target*) adhered over the cortical ROI to the negative lead (also known as *cathode or reference*) adhered to an unrelated area to be examined. If cathodal interaction is not required, the latter electrode can be adhered either as in a bicephalic montage (e.g. vertex or forehead) or extracephalic montage (e.g. shoulder or upper arm) (Datta et al. 2011).

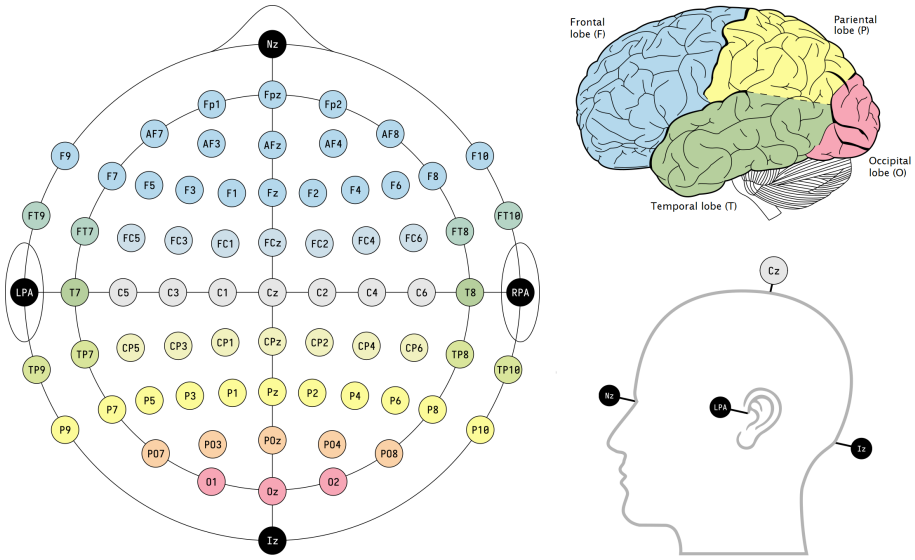

Figure 3.1 *EEG electrode positions in the 10-10 system using modified combinatorial nomenclature as presented by Klem 1999. The electrode sites are colour-coded according to the lobes of the brain which their labels (F, C, P, O, and T) represent. The head indicates the location of the fiducials: the nasion, the (left) pre-auricular point, and the inion.*[1]

3.2 Methods and Dosage

tES incorporates different methodologies which are defined by their dosage, however the definition of 'dose' on this application has been changing for over the past century. Guleyupoglu et al. (2013) present an article with a comprehensive and technical review about historical evolution of tES based on their findings by backtracking research and medical paperwork to the earliest period when documentation refereed to the first studies of electrical stimulation applied on electrosleep and electroanesthesia therapies pairwise (Robinovitch 1914).

For over a century, different electrical stimulation methods and their deviations had been proposed, neglected, resurged and then reshaped into contemporary methods. Herein, four core tES approaches have been intensely explored over the last decade: Direct Current Stimulation (tDCS), Alternating Current Stimulation (tACS), Pulsed Current Stimulation (tPCS), and Random Noise Stimulation (tRNS)

[1] `https://commons.wikimedia.org/wiki/File:EEG_10-10_system_with_additional_information.svg`, by Laurens R. Krol, 20 November 2020, Public Domain.

(Fig. 3.2). These techniques share configuration similarities but the injected current pattern applied and their resulting neuronal behaviour effects differs drastically.

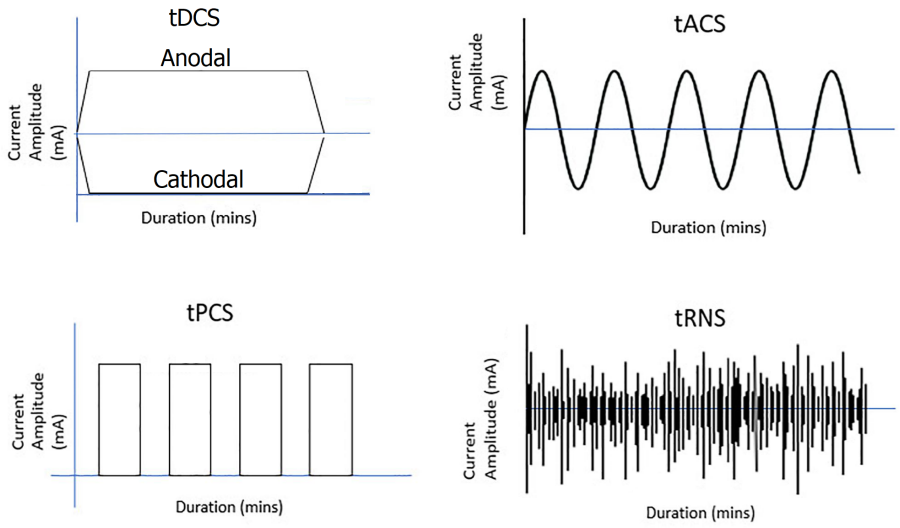

Figure 3.2 *Common transcranial electrical stimulation (tES) waveforms (Current amplitude portrayed is set from -1 to 1 mA).*

3.2.1 Transcranial Direct Current Stimulation (tDCS)

Most predominant and studied method over the last decade, *Transcranial Direct Current Stimulation (tDCS)* is used for modulating cognitive and motor skills in a polarity-dependent manner (Nitsche and Paulus 2000). This method relies upon delivering constant low-intensity currents (0.5-2 mA; Zaghi et al. 2010) throughout the ROI using at least two large patch electrodes (20-35 cm^2 patch size; Moreno-Duarte et al. 2014), which is applied directly to the head, partially penetrates the skull, and enters the brain. tDCS has been successfully employed on healthy subjects to increase cognitive brain function (Nitsche et al. 2003; Kincses et al. 2004; Fregni et al. 2005c) as well as a reliable method for modulating cortical excitability (Nitsche and Paulus 2000) without triggering an action potential (Bikson et al. 2004).

In contrast to the transcranial magnetic stimulation (TMS) methodology, which is able to activate axons via short-pulsed stimulations and establish action potentials, tDCS is incapable to deliver sufficient potential to discharge resting neurons or axons (Nitsche and Paulus 2000). In comparison, the distinguishing electric fields produced by magnetic stimulation are of approximately 100 volts per meter (V/m) while the Direct-Current stimulation offers peaks of 0.3V/m per 1 mA applied. This sustained low-intensity electrical field is capable enough to modulate transmembrane neuronal potentials to bring the underlying neurons close to their firing threshold without bringing up depolarisation (Paulus 2011).

tDCS presents limitations on their own, including the unavailability to target specific frequencies and the lack of focalization using conventional electrodes patches. An increase of applied current pattern higher than 1 mA demands a larger electrode patch (Furubayashi et al. 2008) to mitigate induced skin irritability. In order to compensate the lack of focality, refined methods has been proposed and evaluated. One recently developed method is the "high definition" tDCS (HD-tDCS) approach (Caparelli-Daquer et al. 2012; Borckardt et al. 2012) which replaces the bipolar large electrodes with an array of the smaller electrodes patches (1 cm^2; Moreno-Duarte et al. 2014) narrowing the stimulation area into a specific cortical ROI. As an example, the "4x1 ring" HD-tDCS montage consist of a configuration wherein four electrodes with the same polarity are attached over the target area in the shape of a square and the remaining electrode with opposite polarity is adhered at the center. This HD-tDCS method has delivered more focally-based results compared to the conventional tDCS (Datta et al. 2009) although few HD-tDCS studies have been published.

Figure 3.3 *tDCS electrode montage. Positive lead in red and negative lead in blue.* ***Left****: bicephalic reference.* ***Middle****: extracephalic montage.* ***Right:*** *4x1 HD-tDCS montage.*

3.2.2 Transcranial Alternating Current Stimulation (tACS)

Transcranial Alternating Current Stimulation (tACS) consists on delivering non-constant currents (0.25-0.40 mA; frequencies ranging 1, 10, 15, 30 and 45Hz Antal et al. 2008; electrode patches of size 16cm^2 Moreno-Duarte et al. 2014) which regularly alternates the electrodes flow between positive and negative voltage. The most common method to apply a non-invasive, low-intensity AC current pattern is through biphasic waveforms either in the form of a rectangular wave (intensity reaches a specific amplitude, held at that amplitude for a fixed amount of time, then is interrupted by a current of value zero, start alternating the polarity of the current, repeat the cycle) or in a sinusoidal wave (Zaghi et al. 2010).

AC stimulation alters the transmembrane potential of single neurons based on the polarization of the injected current pattern, for instance, a sinusoidal waveform

leads to sinusoidal fluctuations of the membrane potential. Unlike tDCS, polarization is frequency-dependant and linearly proportional to the injected current; low frequencies induces bigger polarizations than high frequencies.

tACS is used particularly in electroconvulsive therapy as well as eliciting stimulation in deep brain, motor cortex, spinal cord, transcutaneous nerve and vagal nerve (Moreno-Duarte et al. 2014). Furthermore, AC stimulation has the advantage to enable manipulation and physiological neuronal entrainment by alternating transmembrane neuronal potentials through frequency stimulation (Paulus 2011; Thut et al. 2011). The current flow modulated by the anode supplies electrodes over the ROI, promoting endogenous oscillations (*depolarization*) whereas the cathode retracts electrodes, suppressing endogenous oscillations (*hyperpolarization*) (Song et al. 2014)).

3.2.3 Transcranial Pulsed Current Stimulation (tPCS)

Transcranial Pulsed Current Stimulation (tPCS) is another brain stimulating technique within the framework of tES to induce changes over cortical and subcortical brain structures (Datta et al. 2013). This method resembles the previously mentioned tES techniques: similar to tDCS on anode-cathode electrodes relationship, their positioning as well as the possibility to configure a high-definition focality method like HD-tDCS; similar to tACS on the usage of electrode patch size (16 cm^2) and delivering repeated short-bursts of the current rather than sinusoidal waves to induce changes over cortical and subortical brain structures. In addition to the previous aforementioned advantages, tPCS has the opportunity to deliver the current in different classes based on the waveform (function), associate magnitude spectrum (frequency content), and associated clinical references. These classes are Monophasic, Biphasic, Asymmetric, and Pulsed Trains pulses (Guleyupoglu et al. 2013).

3.2.4 Transcranial Random Noise Stimulation (tRNS)

Transcranial Random Noise Stimulation (tRNS) is a relatively new modality that has delivered results yet has not been fully explored. When Terney et al. (2008) investigated this method, they deployed an AC stimulation current in a similar way like tACS, however, instead of delivering at a fixed frequency throughout the session they fluctuated the current at random frequencies levels ranging from 0.1 to 640 Hertz (Hz) for 10 minutes on healthy subjects and discovered a significant excitability increase at the motor cortex using high-frequencies for 60 minutes after-stimulation. Chaieb et al. (2011) conducted a similar study except that they varied the inputs. On this variation, a range of 100 to 640 Hz were used on three sessions

lasting 4, 5 and 6 minutes respectively. Only a minimal duration of 5 minutes session was required to observe the excitability that Terney et al. (2008) presented. While the latter method can be understood as an adjustment, however, comparing the conclusions drawn from both parties are insufficient to determinate whether or not the minimal requirement is indeed only 5 minutes. Even though the physiologically causalities has not been well understood so far, the motivation and results documented are significant enough to be considered as a milestone in tRNS studies. Is suspected that the reason for excitability emanating from this method may be attributed to the repetitive opening of sodium channels (Paulus 2011) or the increased neuronal network sensitivity to modulation (Francis et al. 2003). One advantage worth noticing is that patients have reported to feel less sensations of pain with tRNS compared to the tDCS method.

3.3 Need for Optimization

One pragmatic problem on MC-tES is the amount of freedom researchers and clinicians has for adjusting (tweaking) electrode parameters and current dosage. In most cases, full details are not provided either because focalization over the ROI is enhanced through placement of the electrode on the scalp or the planned injected current for stimulation cannot be delivered (or received) as intended (Guleyupoglu et al. 2013); permitting this action consequently results in an increased number of cases with different adjustments. Although this action can be justifiable since human morphology as well as their electrical properties varies from one case to another, the amount of studies with contradictory outcomes alludes the fact that conventional MC-tES regularization are far from finding optimal standardization.

Conventional tDCS require the usage of extended size electrodes patches to inject the current pattern to a specific area within the target brain ROI. One approach to improve the targeting is to optimize the electrode placement. This optimization varies depends whether the goal is to maximize focality or directionality at the target ROI (Rampersad et al. 2013). Should the goal is to increase the focality, the electrodes patches should be replaced with a dense array of electrodes over the ROI instead (Datta et al. 2009). The availability of using an increased number of electrodes patches consequently leads to an increase of degrees of freedom, thus the importance for devising systematic techniques to determinate optimal injected current pattern is required, specially when using dense arrays as the working area is limited.

4 Forward Modeling

In this chapter, forward problem approach in MC-tES is described. Beforehand, *forward problem* is known as the calculation of electric and magnetic field pattern over a given geometrical model, while an *inverse problem* is the calculation of the time-dependent and position values over the already-measured field pattern (Tanzer 2006). A forward problem is calculated based on a fixed current source, the geometry of the head model and it internal conductivity distribution.

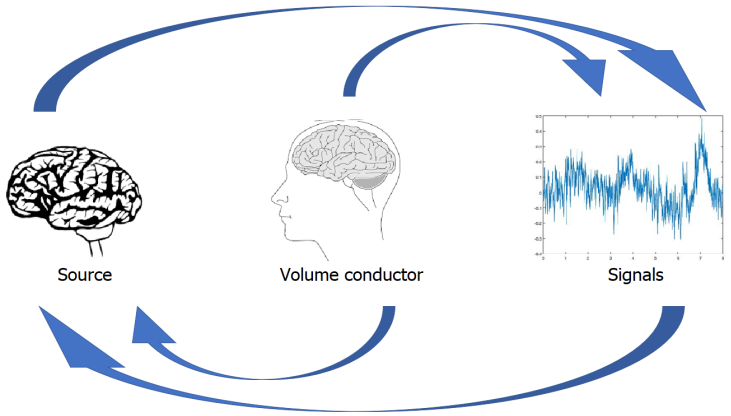

Figure 4.1 *Definitions of forward and inverse problems.*

Modeling the head model is a crucial step in the studies of electromagnetic source imaging. In both EEG and MEG studies, the usage of a spherical model is the most predominant and well-accepted geometric model because it simply reassembles the shape of the human head and demands minimal computational-power for numerical approach. However, relying on information based only on a spherical model is not sufficient for determining source localization, as conductivity is known to be inhomogeneous and anisotropic, i.e. not uniform and properties varies based on direction. For this reason, FEM is applied for modeling both electromagnetic fields and sources within a realistic head model (Pursiainen et al. 2016), as it provides enough flexibility and include detailed conductivity information with great accuracy to solve forward problem.

4.1 Maxwell's equations and quasi-static approach

In order to obtain an appropriate model, basic understanding of electromagnetism is required. *Electromagnetism* is the branch of physics that studies the properties and behaviour of both electric and magnetic fields. Both fields strongly influence each other, therefore, independent study of one field cannot be done without the other.

The electric field can be understood based on Gauss' law contribution. The *Gauss' law* states that any electric charge is capable to produce its own *electric field* $\vec{E}$ and the flux of that field passing through any surface is proportional to the total charge contained within that surface. An electric field (or *E-field*), can be understood as the electrical force $\vec{F}$ exerted on an unit point charge q_0 at any given location, i.e. an interaction experienced by other charges within the field,

$$\vec{E} \equiv \frac{\vec{F}}{q_0} \tag{4.1}$$

By writing in this form, the equation provides us a clear understanding about the following two aspects: first, the electric field is a vector-valued quantity which multiplied by the charge of the particle gives the force of interaction; and second, the resulting units can be re-wrote from newtons per coulomb (N/C) to volts per meter (V/m).

Gauss' law of charge conservation can be expressed for microscopic (differential form) and macroscopic (integral form) fields (Nunez et al. 2006). In the former case, the equations are used to describe every aspect on a detailed dynamic manner even on atomic-level, while the latter field is obtained by applying integral law of Gauss which converts volume integral of a divergence into a boundary integral of a normal component. The differential form in a domain free of monopolar charges, e.g., in a biological tissue, is the following:

$$\nabla \cdot \vec{E} = 0. \tag{4.2}$$

In other words, the divergence of $\vec{E}$ in the domain vanishes, indicating that there are no sources nor sinks in the domain. The macroscopic version obtained as an integral over a closed boundary can be written as:

$$\int_{\partial\Omega} \vec{E} \cdot d\vec{S} = \int_{\Omega} \nabla \cdot \vec{E}\, dV = 0,$$

where $d\vec{S}$ is a surface differential with orientation matching that of the surface normal and length given by the differential surface area. In addition to the Gauss' law, Maxwell's equations includes the Gauss' law for magnetism, Faraday's law and Ampere's circuital law, each one with a differential and an integral form. In the following, we concentrate on the first of these two cases.

The *Faraday's law* states that any magnetic field that interacts with an electrical circuit produces an electromagnetic induction (Sadiku and Sadiku 2001). The Maxwell-Faraday equation, which is a differential form of the Faraday's Law, states that a time-varying magnetic field induces an electromotive force. This law can be

presented as follows:

$$\nabla \times \vec{E} = -\frac{\partial \vec{B}}{\partial t}, \tag{4.3}$$

where $\vec{B}$ is known as the *magnetic flux density*. Since the wavelength of the electromagnetic field is much larger than the diameter of the domain, the behaviour of the electromagnetic field can be assumed to be nearly-static, meaning that the partial derivatives of $\vec{E}$ and $\vec{B}$ with respect of time t are assumed to be zero, i.e., $\partial\vec{E}/\partial t = \partial\vec{B}/\partial t = 0$. This is known as the quasi-static approximation. From Maxwell-Faraday's law it now follows that $\nabla \times \vec{E} = 0$, which shows that the work W_0 per unit charge done by the electric field over any closed path P is zero, since

$$W_0 = \oint_P \vec{E} \cdot d\vec{\ell} = \int_D \nabla \times \vec{E} \cdot d\vec{S} = 0, \tag{4.4}$$

where $d\vec{\ell}$ denotes the differential tangent vector of P and D is a surface enclosed by P. This means that $\vec{E}$ can be expressed as a gradient of a scalar electric potential u as $\vec{E} = -\nabla u$. Now, *Ampere's circuital law*

$$\nabla \times \vec{B} = \mu\left(\vec{J} + \varepsilon\frac{\partial \vec{E}}{\partial t}\right), \tag{4.5}$$

where μ and ε denote the magnetic permeability and the electric permittivity, respectively, can be differentiated side-wise, which yields

$$0 = \nabla \times (\nabla \cdot \vec{B}) = \nabla \cdot (\nabla \times \vec{B}) = \mu\left(\nabla \cdot \vec{J} + \nabla \cdot \left(\varepsilon\frac{\partial \vec{E}}{\partial t}\right)\right) = \mu\nabla \cdot \vec{J}, \tag{4.6}$$

following from the Gauss law for magnetism, i.e., $\nabla \cdot \vec{B} = 0$, the quasi-static approximation, and the assumption that μ is constant (or nearly constant) in a biological tissue. Consequently, Kirchoff's conservation law $\nabla \cdot \vec{J} = 0$ holds for the total current $\vec{J}$ in Ω. The total current can be split into the primary current $\vec{J^p}$ of the brain activity and the volume current $\vec{J^v} = \sigma\vec{E}$. Taking into account that the electric field can be obtained as the negative gradient of the scalar potential, it follows that

$$\nabla \cdot \vec{J} = \nabla \cdot (\vec{J^p} + \vec{J^v}) = \nabla \cdot (\vec{J^p} + \sigma\vec{E}) = \nabla \cdot (\vec{J^p} - \sigma\nabla u) = 0, \tag{4.7}$$

or alternatively, in a simplified form,

$$\nabla \cdot (\sigma\nabla u) = \nabla \cdot \vec{J^p} \tag{4.8}$$

which is the governing partial differential equation for the electric potential in Ω.

4.2 Complete Electrode Model (CEM)

As mentioned in the Chapter 3, electrode properties play an important role in MC-tES. Size and positioning of electrodes influence the focality of the stimulus. For this reason, taking into account electrode modeling is essential for reconstructions. The *point electrode model* (PEM), which is the current standard for EEG, assumes that every electrode in the head model Ω is a neutral, passive-point in the domain Ω, i.e., electrodes do not influence. In contrast, the *complete electrode model* (CEM) (Pursiainen et al. 2012) takes into account the electrode shapes, contact impedance, and *shunting effects*, i.e., alterations of the underlying electric potential due to current circulation on the contact surface (Somersalo et al. 1992; Hanke et al. 2011). Although the differences of these two models has been confirmed to be very small in context of normal EEG (Pursiainen et al. 2012), in this section we explore partial differential equation for electrode modeling as well as the boundary conditions.

In EEG/MEG source analysis, the primary current density $\vec{J^p}$ can be reconstructed through the field measurements on the surface of the head model $\partial\Omega$ (Hämäläinen et al. 1993), however, in the case of MC-tES the simulated electrodes are the only relevant current sources. This means that $\vec{J^p}$ is zero, thus

$$\nabla \cdot (\sigma \nabla u) = 0. \tag{4.9}$$

In order to find an appropriate model for solving 4.9, a head model Ω is stimulated through a montage of $(e_\ell)_\ell$ L electrodes of size $|e_\ell|$. We denote the current applied on the ℓ-th electrode by I_ℓ as well as their potential U_ℓ and impedance Z_ℓ. The boundary conditions for CEM are represented as following:

$$0 = \sigma \frac{\partial u}{\partial n}(\vec{x}), \qquad \text{in} \quad \partial\Omega \backslash \cup_{\ell=1}^{L} e_\ell, \tag{4.10}$$

$$I_\ell = \int_{e_\ell} \sigma \frac{\partial u}{\partial n}(\vec{x}) dS, \qquad \text{for } \ell = 1, 2, \ldots, L, \tag{4.11}$$

$$U_\ell = u(\vec{x}) + \tilde{Z}_\ell \sigma \frac{\partial u}{\partial n}(\vec{x}), \qquad \text{for } \ell = 1, 2, \ldots, L, \ \vec{x} \in e_\ell. \tag{4.12}$$

The first boundary condition describes that no current is flowing inside nor outside of head. The second one states that the total current flux through the ℓ-th electrode equals to the applied current I_ℓ. The third condition describes the relationship between the ungrounded electrode potential U_ℓ and the u potential underneath the electrode. Here, $\tilde{Z}_\ell \sigma \frac{\partial u}{\partial n}(\vec{x})$ is known as the *effective contact impedance*. In this condition, the impedance is a difference that is proportional to 4.11, i.e., the current flux get stronger as the potential differential increases. Additionally, the difference also increases if the effective contact impedance also increases. In the case were

$Z_\ell = 0$ or $I_\ell = 0$, no difference will be present, therefore both potentials U_ℓ and u will become constants, $U_\ell \equiv u$. By assuming that the effective contact impedance is $\tilde{Z}_\ell = Z_\ell |e_\ell|$, we can now rewrite 4.12 as

$$U_\ell = \frac{\int_\ell u \, dS}{|e_\ell|} + Z_\ell I_\ell. \tag{4.13}$$

4.3 Weak Form

A general weak form for electric potential field $u \in H^1(\Omega)$ can be obtained integrating by parts. Here $H^1(\Omega)$ denotes a Sobolev space of square integrable ($\int_\Omega |u|^2 \, dV < \infty$) functions with square integrable partial derivatives. Multiplying 4.9 with a smooth enough test function $v \in S$, where S is a subspace of $H^1(\Omega)$, it follows that

$$\begin{aligned} 0 &= -\int_\Omega \nabla \cdot (\sigma \nabla u) v \, dV, \\ &= \int_\Omega \sigma \nabla u \cdot \nabla v \, dV - \int_{\partial\Omega} \sigma \frac{\partial u}{\partial n} v \, dS, \\ &= \int_\Omega \sigma \nabla u \cdot \nabla v \, dV - \sum_{\ell=1}^{L} \int_{e_\ell} \sigma \frac{\partial u}{\partial n} v \, dS. \end{aligned} \tag{4.14}$$

The weak form of 4.14 can then be obtained by substituting the second term of the right-side and yields

$$\begin{aligned} -\sum_{\ell=1}^{L} \int_{e_\ell} \sigma \frac{\partial u}{\partial n} v \, dS &= -\sum_{\ell=1}^{L} \frac{1}{Z_\ell |e_\ell|} \int_{e_\ell} (U_\ell - u) v \, dS \\ &= -\sum_{\ell=1}^{L} \frac{U_\ell}{Z_\ell |e_\ell|} \int_{e_\ell} v \, dS + \sum_{\ell=1}^{L} \frac{1}{Z_\ell |e_\ell|} \int_{e_\ell} uv \, dS \\ &= -\sum_{\ell=1}^{L} \frac{I_\ell}{|e_\ell|} \int_{e_\ell} v \, dS - \sum_{\ell=1}^{L} \frac{1}{Z_\ell |e_\ell|^2} \int_{e_\ell} u \, dS \int_{e_\ell} v \, dS \\ &\quad + \sum_{\ell=1}^{L} \frac{1}{Z_\ell |e_\ell|} \int_{e_\ell} uv \, dS, \end{aligned} \tag{4.15}$$

thus, the final form is

$$\begin{aligned} 0 &= \int_\Omega \nabla\cdot(\sigma\nabla u)v\,dV - \sum_{\ell=1}^{L}\frac{I_\ell}{|e_\ell|}\int_{e_\ell} v\,dS \\ &- \sum_{\ell=1}^{L}\frac{1}{Z_\ell|e_\ell|^2}\int_{e_\ell} u\,dS\int_{e_\ell} v\,dS \\ &+ \sum_{\ell=1}^{L}\frac{1}{Z_\ell|e_\ell|}\int_{e_\ell} uv\,dS, \end{aligned} \tag{4.16}$$

for all $v \in S$. The left-side of 4.16 defines a diffusion operator. On the right-side, the first term corresponds to neural sources, the second term to the stimulation sources, the third and fourth terms describe the shunting effects.

4.3.1 Point Electrode Model (PEM)

Electrodes that are point-like, for example needle electrodes, can be modelled via PEM evaluating the limit of 4.16, where the surface area of the electrode tends to a single point $\vec{p}_\ell$ (electrode position), that is

$$\frac{1}{|e_\ell|}\int_{e_\ell} v\,dS \to v(\vec{p}_\ell). \tag{4.17}$$

In other words, the integral mean of v tends to $v(\vec{p}_\ell)$. When applied to 4.16, the third and fourth term on the right hand side vanish, since $\frac{1}{|e_\ell|^2}\int_{e_\ell} u\,dS\int_{e_\ell} v\,dS \to v(\vec{p}_\ell)u(\vec{p}_\ell)$ and $\frac{1}{|e_\ell|}\int_{e_\ell} uv\,dS \to v(\vec{p}_\ell)u(\vec{p}_\ell)$. Thus, the weakform for PEM is given by

$$\int_\Omega \sigma\nabla u\cdot\nabla v\,dV = -\int_\Omega(\nabla\cdot J^p)v\,dV + \sum_{\ell=1}^{L} I_\ell v(\vec{p}_\ell) \tag{4.18}$$

4.4 Resistivity matrix

We derive the resistivity matrix $\mathbf{R}$ for the previously mentioned electrode models when the right side of the equation 4.9 has a potential value of zero. Given the scalar valued functions $\psi_1, \psi_2, \ldots, \psi_n \in \mathcal{S}$, the potential $\mathbf{u}$ can be approximated as the finite sum $\mathbf{u} = \sum_{\mathbf{i=1}}^{\mathbf{N}} \mathbf{z_i}\psi_\mathbf{i}$. Denoting by $\mathbf{z} = (z_1, z_2, \ldots, z_N)$ the coordinate vector of the discretized potential, by $\mathbf{U} = (U_1, U_2, \ldots, U_L)$ the (ungrounded) electrode voltages, and by $\mathbf{y} = (I_1, I_2, \ldots, I_L)$ as the injected current pattern, the weak form 4.16 is given by

$$\begin{pmatrix} \mathbf{A} & -\mathbf{B} \\ -\mathbf{B}^T & \mathbf{C} \end{pmatrix}\begin{pmatrix} \mathbf{z} \\ \mathbf{y} \end{pmatrix} = \begin{pmatrix} \mathbf{0} \\ \mathbf{U} \end{pmatrix}. \tag{4.19}$$

Here, $\mathbf{A}$ is of the form

$$a_{i,j} = \int_\Omega \sigma \nabla \psi_i \cdot \nabla \psi_j \, dV + \sum_{\ell=1}^{L} \frac{1}{Z_\ell |e_\ell|} \int_{e_\ell} \psi_i \psi_j \, dS, \tag{4.20}$$

and the entries of $\mathbf{B}$ (N-by-L) and $\mathbf{C}$ (L-by-L) are given by

$$b_{i,\ell} = \frac{1}{Z_\ell |e_\ell|} \int_{e_\ell} \psi_i \, dS, \tag{4.21}$$

$$c_{\ell,\ell} = \frac{1}{Z_\ell}. \tag{4.22}$$

Consequently, the resistivity matrix satisfying $\mathbf{z} = \mathbf{R}\mathbf{y}$ can be expressed as

$$\mathbf{R} = \mathbf{A}^{-1}\mathbf{B}(\mathbf{C} - \mathbf{B}^T\mathbf{A}^{-1}\mathbf{B})^{-1}. \tag{4.23}$$

The ungrounded electrode potentials $\mathbf{U}$ can be obtained by referring to the bottom row of 4.19, $\mathbf{U} = -\mathbf{B^T z} + \mathbf{C y}$. The resistivity matrix for the PEM weak form 4.18 can be followed from 4.23 by taking the limit $|e_\ell| \to \vec{p}_\ell$ which leads to

$$b_{i,\ell} \to \frac{1}{Z_\ell} \psi_i(\vec{p}_\ell) \tag{4.24}$$

and

$$a_{i,j} \to \int_\Omega \sigma \nabla \psi_i \cdot \nabla \psi_j \, dV + \sum_{\ell=1}^{L} \frac{1}{Z_\ell} \psi_i(\vec{p}_\ell) \psi_j(\vec{p}_\ell) \tag{4.25}$$

or

$$a'_{i,j} \to \int_\Omega \sigma \nabla \psi_i \cdot \nabla \psi_j \, dV. \tag{4.26}$$

4.5 Volume current matrix

We now define a matrix $\mathbf{F}^{(k)}$ which evaluates the k-th Cartesian component of the volume current density $-\sigma \nabla u$ when multiplied by the coordinate vector $\mathbf{z}$ of the discretized electrical potential distribution u. The entries of this matrix are given by

$$f_{i,j}^{(k)} = \begin{cases} -\sigma_j (\nabla \psi_j)_k, & \text{if} \quad j \in T_i \\ 0, & \text{otherwise,} \end{cases} \tag{4.27}$$

where subsets T_i, $i = 1, 2, \ldots, M$ form a partitioning of Ω for a user-defined dimension M. The k-th Cartesian component of the discretized volume current given the stimulating current pattern can be obtained as follows

$$\mathbf{F}^{(k)}\mathbf{R}\mathbf{y} = \mathbf{F}^{(k)}\mathbf{A}^{-1}\mathbf{B}(\mathbf{C} - \mathbf{B}^T\mathbf{A}^{-1}\mathbf{B})^{-1}\mathbf{y}. \tag{4.28}$$

Further, we define lead field matrix of MC-tES as follows:

$$\mathbf{L} = \begin{pmatrix} \mathbf{F}^{(1)} \\ \mathbf{F}^{(2)} \\ \mathbf{F}^{(3)} \end{pmatrix} \mathbf{A}^{-1}\mathbf{B}(\mathbf{C} - \mathbf{B}^T\mathbf{A}^{-1}\mathbf{B})^{-1}, \tag{4.29}$$

which maps the current pattern linearly to the volume current as given in 4.28. This can be considered as the *forward mapping* in the process of optimizing the current pattern given a targeted discretized primary current distribution $(\vec{J^p})_k = \sum_{i=1}^{M} {x_i}^{(k)}(\vec{w_i})_k$ associated with the coordinate vector $\mathbf{x}^{(k)} = ({x_1}^{(k)}, {x_2}^{(k)}, \ldots, {x_M}^{(k)})$.

5 Optimization Procedure

As mentioned in chapter 3, subjects that had underwent to brain stimulation sessions have reported sensations of skin irritation where electrodes had been attached to. As a response, we investigate for a method that can help us understand how to reduce this uncomfortable characteristic by analyzing the possibility to reduce or mitigate the total amount of potential emanating from the electrodes and, as consequence, reducing global maximum and minimum levels of current required. This reduction can be approached through ℓ_1 *regularization*, a method used for finding unique solutions to ill-posed problems by intentionally adding information to the absolute value of the weight in order to make a less complex model. We concentrate on the following minimization problem

$$\arg\min_{\mathbf{y}}\{\, \|\mathbf{L}\mathbf{y}-\mathbf{x}\|_1 + \alpha\|\mathbf{y}\|_1 \,\} = \arg\min_{\mathbf{y}} \|\mathbf{G}\mathbf{y}-\mathbf{s}\|_1\,, \tag{5.1}$$

where

$$\mathbf{x} = \begin{pmatrix} \mathbf{x}^{(1)} \\ \mathbf{x}^{(2)} \\ \mathbf{x}^{(3)} \end{pmatrix}, \quad \mathbf{G} = \begin{pmatrix} \mathbf{L} \\ \alpha \mathbf{1}^{\mathbf{T}} \end{pmatrix}, \quad \mathbf{s} = \begin{pmatrix} \mathbf{x} \\ \mathbf{0} \end{pmatrix}, \quad \text{and} \quad \mathbf{1} = \begin{pmatrix} 1 \\ 1 \\ \vdots \\ 1 \end{pmatrix}$$

$\mathbf{x}$ is a given discretized primary current distribution, $\mathbf{y}$ is a current pattern, $\mathbf{L}$ a mapping between those, and α is a regularization parameter that suppress the components of the injected current amplitude for setting the MC-tES current amplitude allowed. By minimizing the right side of 5.1 we aim at calculating a current pattern and a volume current distribution which yields minimal non-zero entries. This is advantageous for localizing the stimulus in the brain and to minimize the total amount of dosage given to the subject.

$$\arg\min_{\mathbf{y}} \sum_i |\sum_j G_{i,j} y_j - s_i| = \arg\min_{\mathbf{y}} \sum_j \sum_i G_{i,j}\, y_j - \sum_i s_i \quad \text{with} \quad \mathbf{G}\mathbf{y} \geq \mathbf{s}. \tag{5.2}$$

Defining $\mathbf{g}$ with $g_j = \sum_i G_{i,j}$ this can be formulated as

$$\arg\min_{\mathbf{y}} \mathbf{g}^T\mathbf{y} \quad \text{with} \quad \mathbf{G}\mathbf{y} \geq \mathbf{x}, \tag{5.3}$$

5.1 Linear Programming

A linear programming problem consist of a problem of maximizing or minimizing a linear function subject to linear constraints. In this context, the problem is to find

optimal α regularization parameter which can minimize $\mathbf{y}$ current distribution over the electrodes by

$$\arg\min_{\mathbf{y}} \mathbf{g}^T\mathbf{y} \quad \text{with} \quad \begin{cases} -\mathbf{G}\mathbf{y} \leq -\mathbf{x}, \\ \mathbf{1}^T\mathbf{y} = 0, \\ \mathbf{y}_{\text{lower}} \leq \mathbf{y} \leq \mathbf{y}_{\text{upper}}. \end{cases} \tag{5.4}$$

where $\mathbf{g}$, $\mathbf{y}$, $\mathbf{y}_{lower}$, $\mathbf{y}_{upper}$, $\mathbf{x}$, $\mathbf{1}^T$ are vectors, and $\mathbf{G}$ as matrix. $\mathbf{y}_{lower}$ and $\mathbf{y}_{upper}$ are considered as the *lower bound* and *upper bound* of $\mathbf{y}$, respectively. Now, we proceed to minimize this equation using mathematical optimization methods.

In mathematical optimization, *duality* refers that any optimization problem may be evaluated from within two perspectives, the *primal problem* or *dual problem* (Boyd and Vandenberghe 2004). The *dual-simplex algorithm* essentially consists of performing a simplex algorithm on the latter problem whose obtained solution shall provide a lower bound value to the solution of the former problem. First, the algorithm perform a preprocessing procedure:

- Converts all lower bounds values into zeros.
- Validate the existence of upper bound ($\mathbf{y}_{upper}$) and lower bound ($\mathbf{y}_{lower}$) on any variable. If this holds true, check for feasibility.
- Validate linear equalities and inequalities on any variable. If this holds true, check for feasibility: remove the variable for equalities, and change the constraint to be a boundary for inequalities.
- Remove any empty rows in the linear constraint matrix.
- Determine the consistency of the bounds and linear constraints.
- Validate if any of the variables appear only as linear terms in the objective function and not in any linear constraint. If this holds true, check for feasibility and boundedness, then fix the variables at their appropriate bounds.
- If an inequality constraint is found, a *slack variable* is added to the inequality constraint to transform the constraint into an equality.
- In the case that neither a possible solution or an unbounded problem can be found, the algorithm continues until reaching a stopping criteria. Once met, it will undo all transformations and reconstructs back the original problem.

Once the preprocessing steps are done, the problem 5.4 is reduced to

$$\arg\min_{\mathbf{y}} \mathbf{g}^T\mathbf{y} \quad \text{with} \quad \begin{cases} -\mathbf{G}\mathbf{y} = -\mathbf{x}, \\ 0 \leq \mathbf{y} \leq \mathbf{y}_{upper}, \end{cases} \tag{5.5}$$

where in this form $\mathbf{G}$ and $\mathbf{x}$ are the transformed constraint matrices of their original versions with the upper bounds constrains included in the former matrix. If slack variables are required to be added due to inequality constraints, then the equation 5.5 is written as

$$\arg\min_{\mathbf{y}} \mathbf{g}^T\mathbf{y} \quad \text{with} \quad \begin{cases} -\mathbf{G}\mathbf{y} = -\mathbf{x}, \\ \mathbf{y} + \mathbf{s}_{primal} = \mathbf{y}_{upper}, \\ \mathbf{y} \geq 0, \mathbf{s}_{primal} \geq 0, \end{cases} \tag{5.6}$$

where $\mathbf{s}_{primal}$ are the *primal* slack variables. This is known as the *primal problem* of the dual-simplex algorithm. To solve the *dual problem* of the dual-simplex algorithm, the algorithm requires to solve the equation

$$\max -\mathbf{x}^T\mathbf{v} - {\mathbf{y}_{upper}}^T\mathbf{w} \quad \text{with} \quad \begin{cases} -\mathbf{G}^T\mathbf{v} - \mathbf{w} + \mathbf{s}_{dual} = \mathbf{g}^T \\ \mathbf{s}_{dual} \geq 0, \mathbf{w} \geq 0. \end{cases} \tag{5.7}$$

where $\mathbf{v}$ and $\mathbf{w}$ are the *dual* variables and $\mathbf{s}_{dual}$ are the *dual* slack variables. The optimum conditions that can satisfy both primal equation 5.6 and dual equation 5.7 are

$$\mathbf{F}(\mathbf{y}, \mathbf{v}, \mathbf{s_{dual}}, \mathbf{s_{primal}}, \mathbf{w}) = \begin{pmatrix} -\mathbf{G}\mathbf{y} = -\mathbf{x} \\ \mathbf{y} + \mathbf{s}_{primal} - \mathbf{y}_{upper} \\ -\mathbf{G}^T\mathbf{v} - \mathbf{w} + \mathbf{s}_{dual} - \mathbf{g}^T \\ \mathbf{y_i s_{dual}} \\ \mathbf{s}_{primal}\mathbf{w}_i \end{pmatrix} = \mathbf{0}, \tag{5.8}$$

$$\mathbf{y} \geq 0, \mathbf{s}_{dual} \geq 0, \mathbf{s}_{primal} \geq 0, \mathbf{w} \geq 0, \tag{5.9}$$

where $\mathbf{y}\mathbf{s}_{dual}$ and $\mathbf{s}_{primal}\mathbf{w}$ are component-wise multiplications. 5.7

5.1.1 Implementation for MC-tES in Zeffiro Interface

We devised a function in Zeffiro Interface (`zef_optimize_tes_current.m`) designed to formulate all variables in 5.4 in order to be used on MATLAB function '*linprog*' from the optimization toolbox. The input arguments required are the $\mathbf{L}$ projections, the $\mathbf{x}$ discretized primary current distribution, and a third variable-length argument (*varargin*) which contains the tolerances and stopping criteria for the solver, i.e., limits which stops the solver when are exceeded. The latter argument should contain the following list of variables: (1) a variable that represents the total number of active electrodes applied in $\partial\Omega$, (2) a variable that defines the lower bound ($\mathbf{y}_{lower}$) and upper bound ($\mathbf{y}_{upper}$), (3) a variable that sets the regularization parameter (α), (4)

a variable that defines the termination tolerance on function value (*TolFun*), (5) a variable that defines feasibility tolerance for constraints (*TolCon*), and (6) a variable that sets the optimization algorithm (in this case, 'dual-simplex').

5.2 Numerical experiments

5.2.1 Head model description

As mentioned in chapter 4, generating a FE mesh of a spherical model for studying partial differential equations is generally known to be a reliable approximation for studying the human head due to the simplicity of the geometrical properties generated compared against the subject's morphological topography. A distinctive feature of using a sphere is the low-cost computational power requirement for calculating lead field as well as analyzing data simulation and mathematical modeling. A *lead field* is an electric current field in the volume conductor generated by feeding a unit current to the head (Malmivuo et al. 1997). The first test of the present implementation was conducted using a spherical model. However, since the optimization process here is highly dependant on the local geometry of the head, the numerical experiments concentrate on a realistic model.

In the case of a realistic head model, the volume conductor is based on openly available[1]anatomical magnetic resonance imaging (MRI) data obtained for a real subject. The lead field generation takes into account multiple different tissue layers including, most importantly, white matter, grey matter, cerebrospinal fluid, scalp and skull with have complex geometrical properties specific to the subject. Furthermore, each tissue's conductivities influence on the accuracy of model for the forward solution (Montes-Restrepo et al. 2014). As the reference conductivity values we use the set proposed in (Dannhauer et al. 2011).

In this thesis project, the FEM mesh and lead field of the realistic head model were calculated using ZI after segmenting the MRI data with the FreeSurfer software and importing the resulting ASCII files. The mesh resolution of 1 mm was used in order to obtain physiologically accurate results (Rullmann et al. 2009).

5.2.2 Synthetic sources and placement

The electric potential generated by neurons can be modeled as dipoles. In electromagnetism, an electric *dipole* represents the separation distance between two charges of equal and opposite value within any electromagnetic system (Brau 2003). The

[1]`https://brain-development.org/ixi-dataset/`, Biomedical Image Analysis Group, Imperial College London

generated electric field lines by the dipole emanate from the positive charge, travelling through a medium, and converging on the negative charge of the same dipole. In the brain, voltage variation at the scalp resulting from current flow can be measured through EEG. The MC-tES method can simulate this variation via multiple current injections on the scalp, the volume current distribution corresponding to this variation is to be fitted with the dipolar source.

In Zeffiro Interface, one can simulate the dipoles as *dipolar synthetic sources* and visualize them in the head model. Hence, one can analyze the effects of the current patterns by comparing the volume current distribution to the dipole to obtain a range of parameters that can provide the best match between synthetic dipole and the volume current density. The present numerical experiments consider finding a minimal current pattern corresponding to a dipolar source designated within each of the following three brain areas on the left hemisphere: the somatosensory area in the pariental lobe, visual area in the occipital lobe, and auditory area in the temporal lobe. ZI presents a parcellation tool (based on 36-label Desikan killiany) which can be used to display and distinguish these regions as in Fig. 5.1.

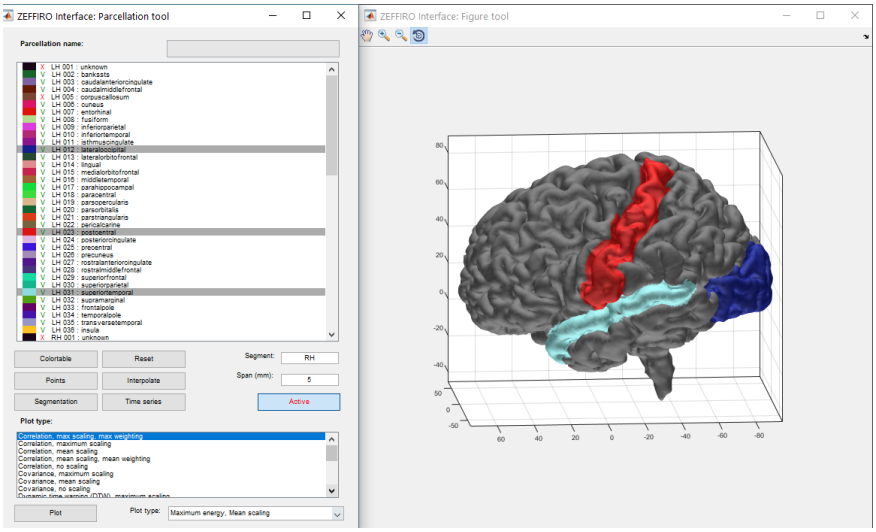

Figure 5.1 *Zeffiro Interface parcellation tool and figure tool. Visible grey matter with postcentral gyrus in the pariental lobe in red, lateral occipital lobe in blue, and superior temporal gyrus in superior temporal lobe in cyan.*

A *gyri* appears as a ridge on the surface of the brain while the *sulci* appears as trench-looking depression or fissure (Fig.5.2(a)). Together they make up the folded surface of the cerebral cortex. Based on the Brodmann's areas (Brodmann 2007), source dipoles are defined as close as possible to the postcentral sulcus in the pariental lobe, transverse occipital sulcus in the occipital lobe, and the superior temporal sulcus in the temporal lobe (Fig.5.2(b)). These sources will emanate the current pattern (nAm) across the realistic head model.

Using ZI forward tools, the Cartesian components of the sources are indicated in order to allocate the source geometrically next to the selected sulcus. For visualization purposes, sources are represented in ZI figure tool as circles with a line pointing away from the center indicating the orientation at which the elicited strength of the source is pointing to in a coordinate system. Additionally, more than one source can be simulated at the same time by declaring the previously mentioned values in the same forward tools window.

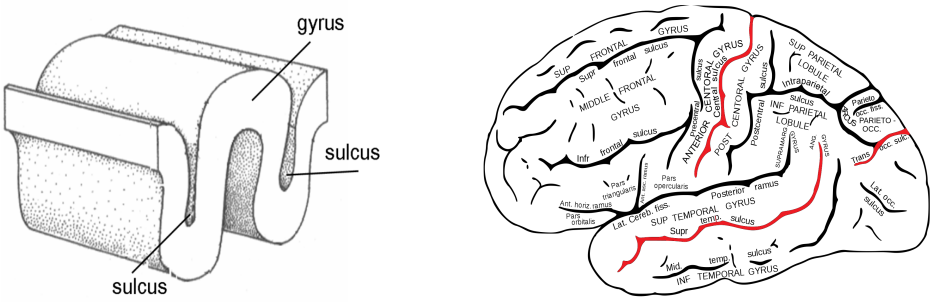

(a) Gyrus and sulcus.

(b) Sulcus of interest.

Figure 5.2 *Representation of gyrus and sulcus; lateral surface of the left cerebral hemisphere with postcentral sulcus, transverse occipital sulcus, and superior temporal sulcus highlighted in red.*[2]

Once a source and the parametric structure for the optimization described on 5.1.1 has been officially established the calculations can take place. In the following experiments, a synthetic dipolar source of value 10 nAm source is placed in three different target areas (somatosensory, visual and auditory) inside the brain. The reference source extent is set to be $40^{3/2} \approx 253$ mm^3 which is the volumetric correspondent of the typical value 40 mm^2 suggested in Hari and Puce 2017. The maximal strength of the stimulus current is chosen to be ± 2.0 mA which is known to be generally tolerable in tES.

5.2.3 Numerical optimization approach: general, regularized and active cases

In the optimization process, the dual-simplex linear programming algorithm is executed repeatedly for a total of m-by-n times, setting different values for the tolerance of the residual norm and the regularization parameter 5.4: m is the length of a positive vector containing a range of termination tolerance values, and n is the length

[2] 5.2(a), (`https://commons.wikimedia.org/wiki/File:Gyrus_sulcus.png`) by Albert kok, 24 May 2007, Public Domain. 5.2(b), (`https://commons.wikimedia.org/wiki/File:Gray726.png`) by Henry Gray (1825–1861). Anatomy of the Human Body, 1918, Public Domain.

of another positive scalar with α values. The values within the scalars

$$m = (1e^{-4}, 1e^{-5}, \ldots, 1e^{-10}), \quad \text{and} \quad n = (0, 1e^{8}, 1e^{9}, \ldots, 1e^{15})$$

are based on the optimization option structure criteria from MATLAB optimization toolbox. These values refer to a system obtained in SI-units. Each m-th value is used as a lower bound on the change in the value of the objective function during a linear program step, i.e., if the termination tolerance of the function $m(1 + \|g^T(y_m)\|) > \|g^T(y_m) - g^T(y_{m+1})\|$ the iteration ends. The n-th values represents the amount of regularized penalty that is added to G prior each iteration. The outputs of the Zeffiro Interface function, including the parametric structure, and the amount of elapsed time required per iteration (in seconds), are all recorded under the surname *results general* using m and n values as matrix index indicators (i.e., a *struct* featuring *cells* matrices, each cell contains the resulting current pattern, residual, flag values, and elapsed time per iteration, individually). Whenever a feasible solution is found, the $\mathbf{y}_{(m,n)}$ values are subject for further examination.

Another approach that supports our study is the calculation of the optimization terms over a reduced montage version. When a feasible solution has been found, the discretized electrode potentials values within $\mathbf{y}_{(m,n)}$ that are close to zero can be distributed among the other electrodes with the purpose for enhancing sparsity. When an electrode potential does not meet the $\mathbf{t}$ percentage threshold criteria, being $\mathbf{t}$ a vector containing threshold values for the algorithm ($\mathbf{t} = 12.5\%$ and 25%) the electrode potential at the given (m, n) instance is set to zero. This thresholded result is registered as $\mathbf{y}_{(m,n,t)}$, where $\mathbf{t}$ is the third cell matrix indicator representing the amount of percentage used. Along with their residual, the new results are recorded in an independent struct named *results threshold*. The generated current pattern $\mathbf{y}_{(m,n,t)}$ is used on 5.4 for evaluating a new set of optimization terms in a now-segregated montage. The obtained results based on the previous indications are recorded as *results active* using the same nomenclature of matrix index indicators already described.

It is important to mention that when no feasible solution is found at each iteration, the ZI function returns zero for all the numerical values and the flag value is set to indicate that no solution was found under the given parameters. A zero, in this manner, does not affect upon the determination of minimal values. The code used in the optimization tests of this thesis is included as an appendix.

6 Results

Once the algorithm described in section 5.1.1 is done searching for feasible solutions comparison of which combination of optimization terms yields the minimal amount of amperage (mA) distributed for a 128 active electrode montage used in ZI. Following the recommended maximum amperage allowed for tDCS stimulation sessions (Nitsche 2003), the maximum amperage is set to ± 2.0 mA. In order to illustrate how much α can compliment or deteriorate the results we compare the current pattern distribution of a non-regularized version against a regularized version. A non-regularized version is obtained when n is set to the first scalar value, i.e., α equals to zero. A regularized version corresponds to the results obtained using the indicators m and n set to the matrix cell where the lowest amount of normalized potential is located. Furthermore, we analyze the distribution differences between the general version of the regularized version against their thresholded version, and active montage-reduced version. Additionally, the general, threshold, and active reconstructions and topographies for each case are also presented.

6.1 Case I - Somatosensory Cortex

For analysing the current density at the somatosensory cortex and surroundings, the postcentral gyrus has been highlighted with red color. The synthetic source dipole is displayed with green color, summoned at coordinates (-40,-27,67) and with orientation (0,1,0) indicating that the current flow from this dipole shall travel in the direction as represented in Fig. 6.1.

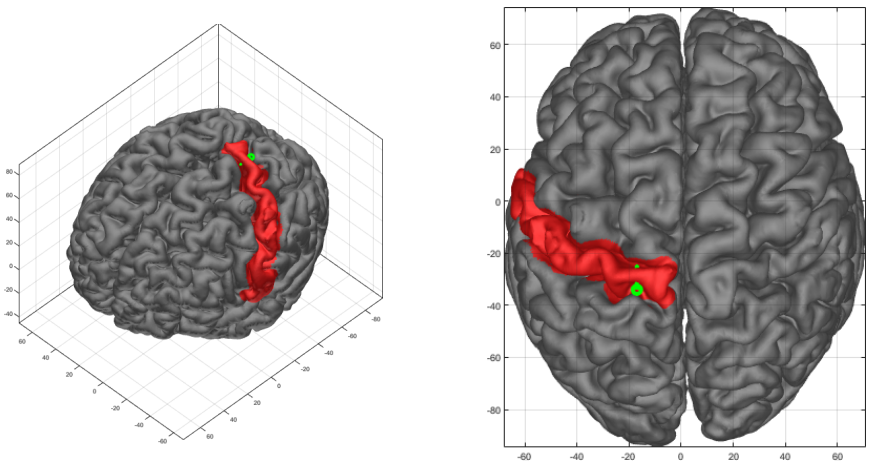

Figure 6.1 *Parcellation of left hemisphere postcentral gyrus (red). Synthetic source (green dot) positioned at postcentral sulcus.*

Once the dipole has been set and all the calculations are done, comparing the results each combination of termination tolerance and penalty term provides by plotting an scaled-color image. The levels of brightness at each cell represents the amount of total electric potential obtained from the calculated current pattern. Additionally, the scaled-color values of active results of both 12.5% and 25% are also displayed in Fig. 6.2. Out of the obtained 63 cases (7-by-9), the terms that yields the minimal potential are when the maximum absolute sum of current values and residuals are closest to zero (green dot).

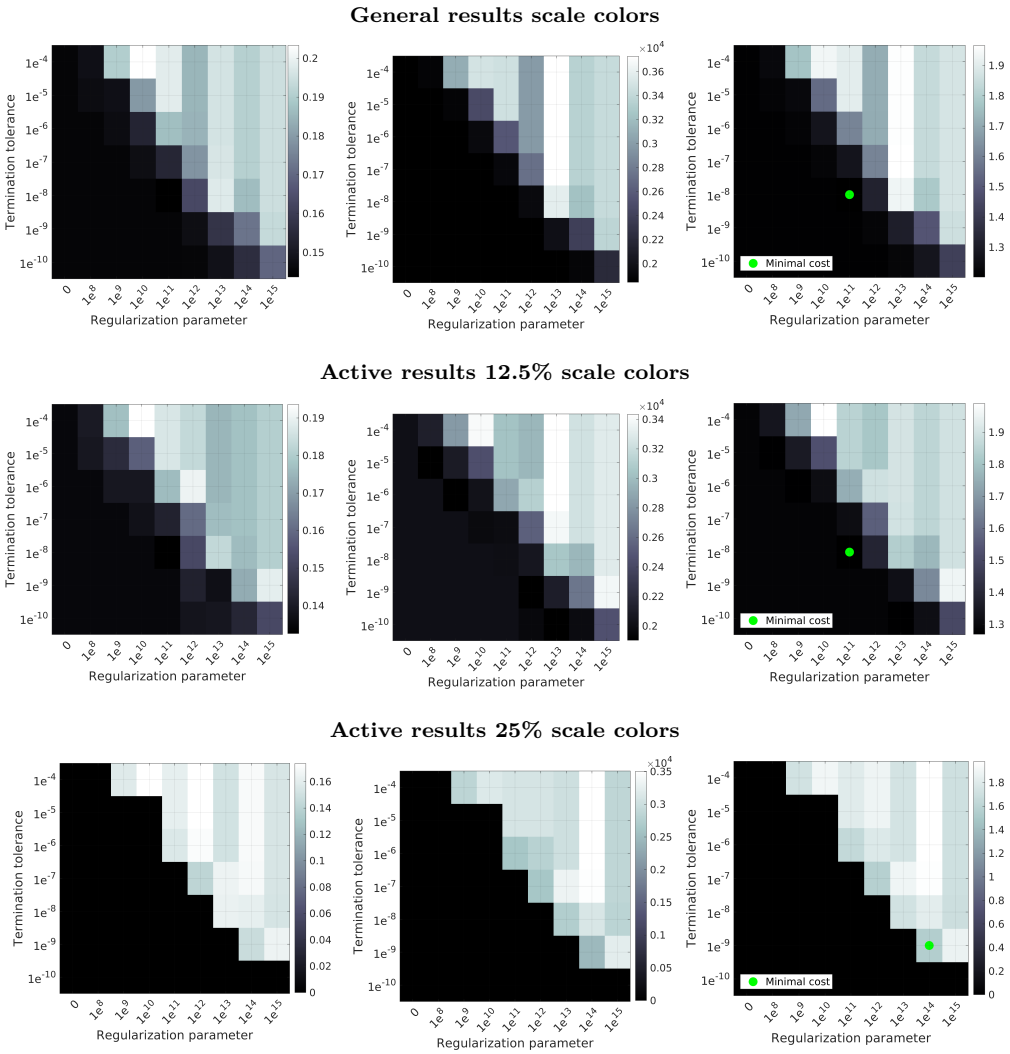

Figure 6.2 *scaled-color representations of the normalized results based on regularization parameter and termination tolerance.* ***Left:*** *Current values (y).* ***Middle:*** *Residual values.* ***Right:*** *Maximum absolute sum of current values and residuals. Minimal cost highlighted as a green dot.*

On the general version, minimal cost is obtained when both termination tolerance and regularization parameter are set on the fifth scalar value of m vector and n vector respectively ($TolFun = 1e^{-8}$, $\alpha = 1e^{11}$). Using these two terms,

the linear programming solver yields a normalized current pattern with minimal cost as $min\|\mathbf{y}_{(5,5)}\|_1 = 1.2016$ mA. We compare the electrode potentials from a non-regularized version ($\alpha = 0$) against the calculated optimum regularized version (Fig. 6.3).

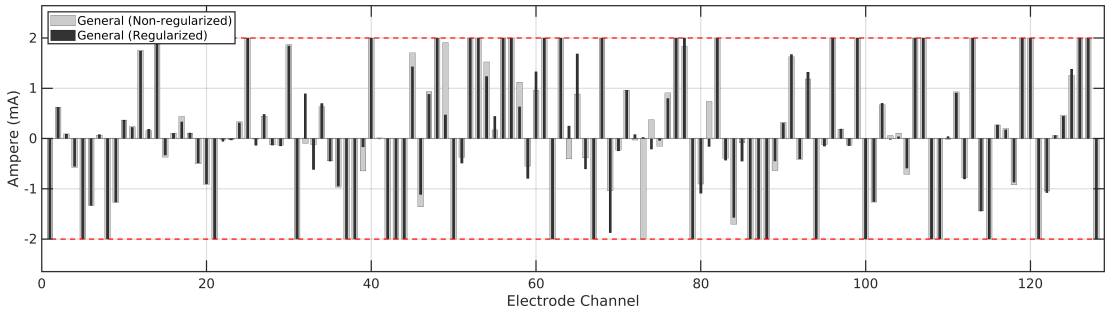

Figure 6.3 *Comparison of non-regularized and optimum regularized current pattern distribution across the 128 channels with synthetic source dipole at the postcentral sulcus.*

Using the minimal feasible solution possible, we now calculate their 12.5% reduced montage version. Based on the linear programming results, neither termination tolerance or α parameters have changed after the re-calculations, i.e., the m and n scalar values are the same. Consequently, as the channels were filtered due to their low values the amount of electric potential is now distributed over the remaining channels resulting in an increase of amperage. Normalizing the results (Fig. 6.2) we obtain an increased value of $min\|\mathbf{y}_{(5,5,1)}\|_1 = 1.2689$ mA.

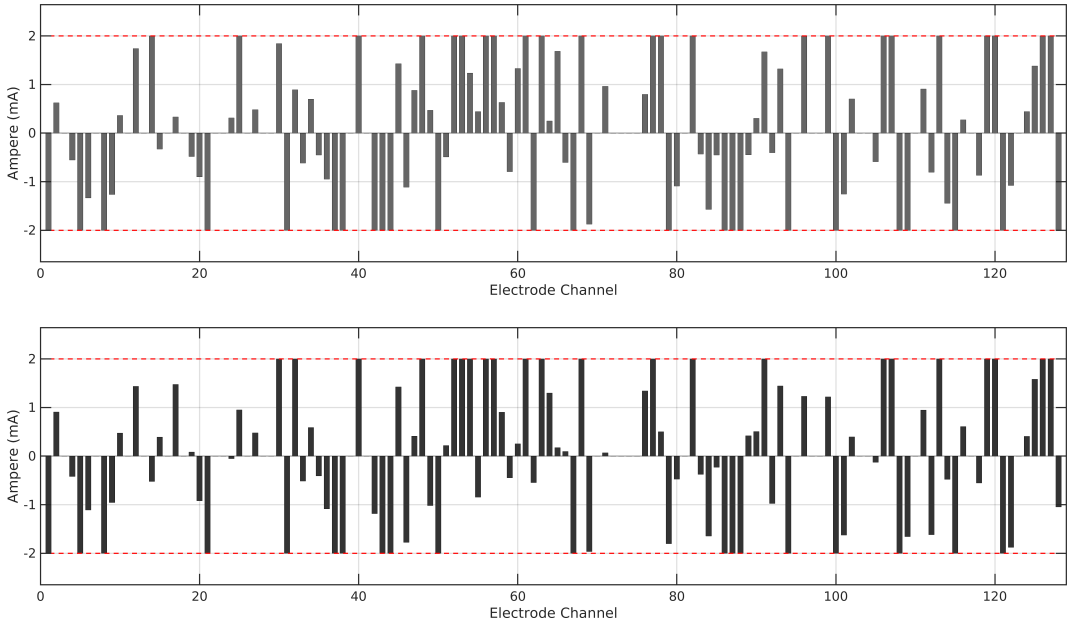

Figure 6.4 ***Top****: Thresholded regularized current pattern distribution (12.5%).* ***Bot****: Active reduced montage current pattern distribution.*

When the threshold value is further increased to 25%, the number of available channels is drastically reduced to the point where sparsity is barely affordable due to the difficulties for finding feasible solutions. Under these circumstances, an increased termination tolerance and penalization term is required to allow the linear programming solver to find viable non-zero optimal solution. The minimal possible solution that can be obtained is when $TolFun = 1e^{-9}$ and $\alpha = 1e^{14}$ (Fig. 6.2). For these terms the solution is $min\|\mathbf{y}_{(6,8,2)}\|_1 = 1.5494$ mA.

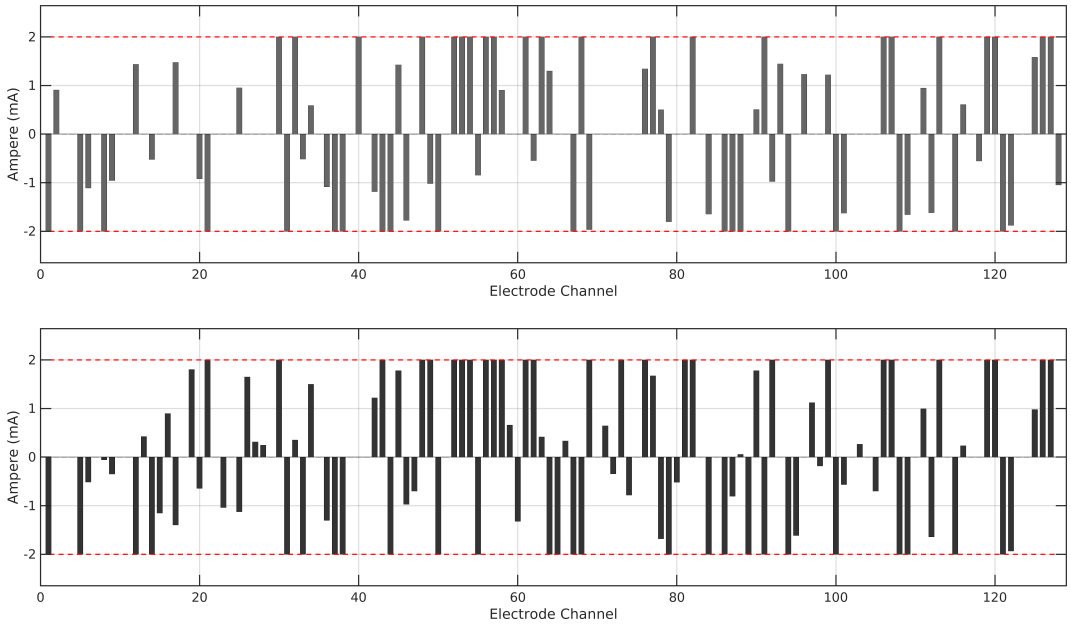

***Figure 6.5 Top**: Thresholded regularized current pattern distribution (25%). **Bot**: Active reduced montage current pattern distribution.*

We now proceed to compare the regularized current distributions against the reduced variations obtained (refer to Fig. 6.6). The 12.5% version resembles to the original method in terms of active/inactive electrodes needed while the 25% version demands a setup where some of the electrodes require inverted polarities (e.g. first 20th electrodes and 40th to 50th electrodes).

Reconstruction and topographies displaying the strength of the electric field are distinguished from the intensities of color distributed across the matter (Fig. 6.7). Unquestionably, the highest energy field concentration is where the source has been initially declared. From this point forward, the strength gradually diminishes as it travels through the boundaries in a bidirectional fashion: posteroanterior towards the frontal lobe, and inferolateral of the pariental lobe on the right hemisphere. For this reason, sparsity optimization can be harshly obtained. This effect can be noticed when comparing the threshold 25% reconstruction.

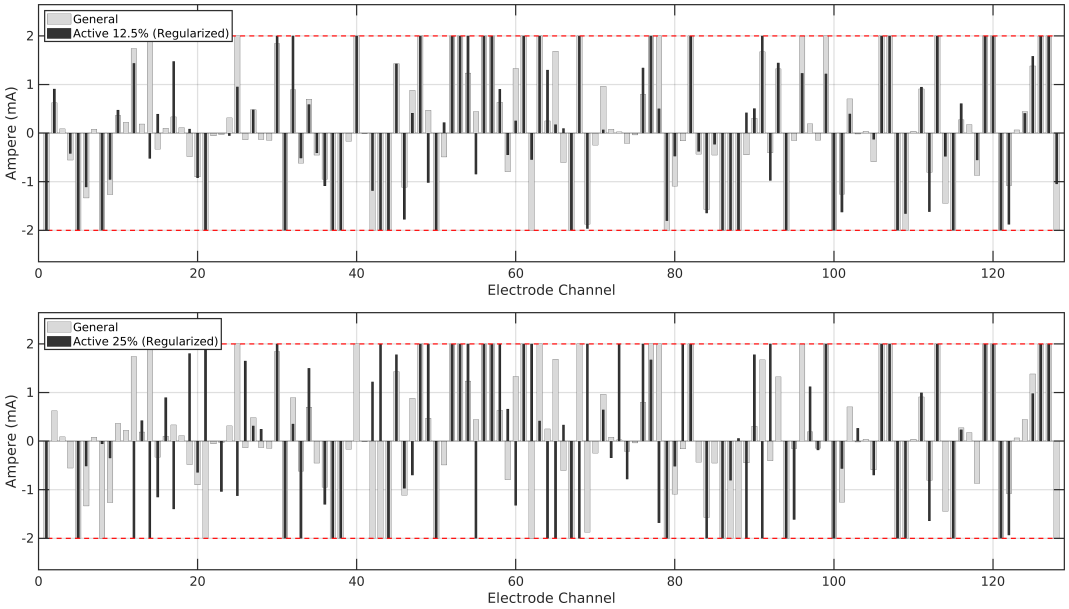

Figure 6.6 *Comparison of active current pattern distribution.* ***Top:*** *General regularized and reduced 12.5% version.* ***Bottom:*** *General regularized and reduced 25% version.*

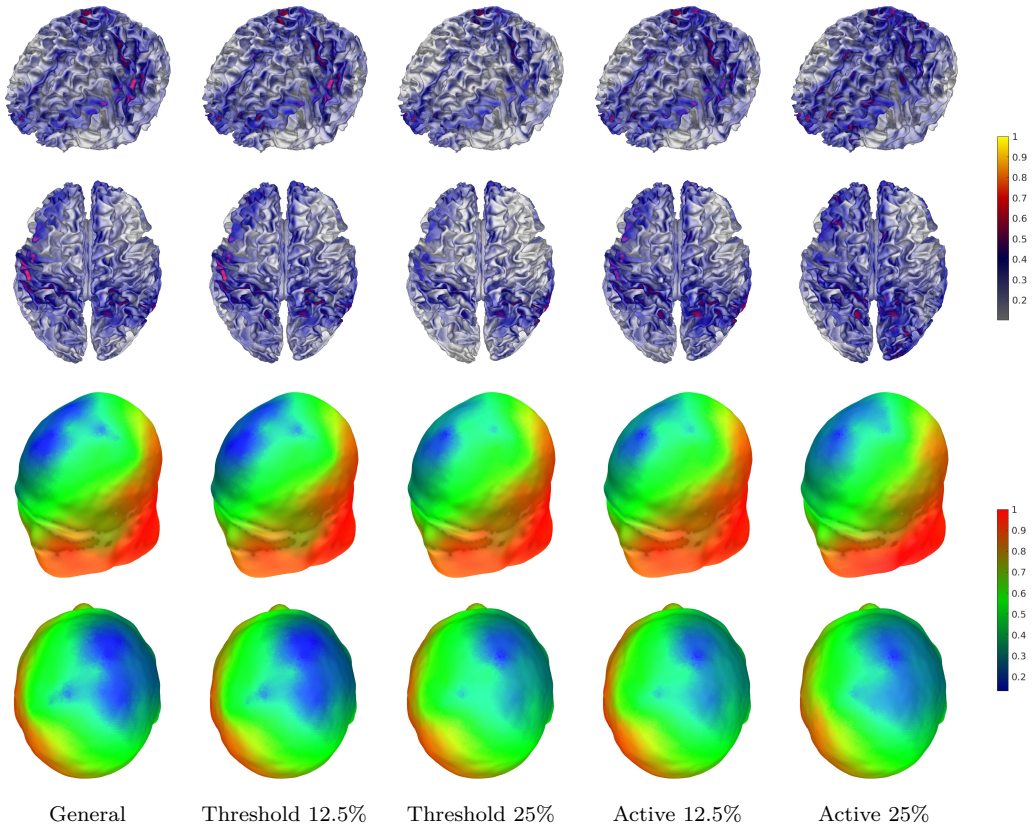

Figure 6.7 *Reconstructions and topographies using optimum tolerance and regularization with dipole simulated at the postcentral sulcus, left hemisphere.*

6.2 Case II - Visual Cortex

Following the same procedure as the 6.1 case, the occipital lobe is highlighted with blue color. The source is displayed with green color, position coordinates are set at (-15,-90,20) with direction coordinates are set as (0,1,0) wherein the transverse occipital sulcus can be located as shown in Fig. 6.8.

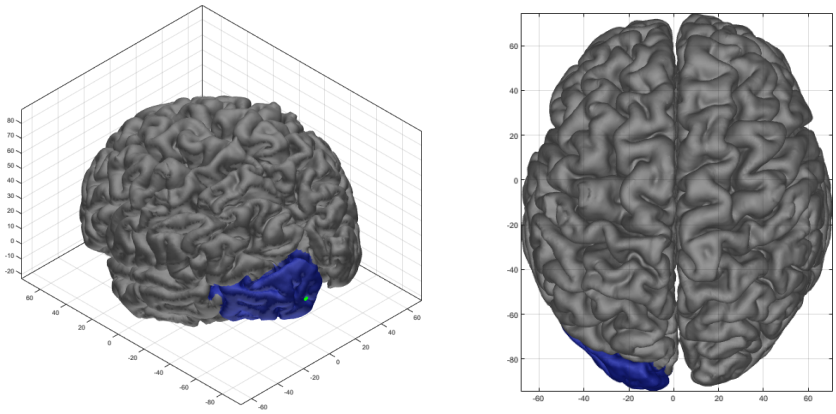

Figure 6.8 *Parcellation of left hemisphere occipital lobe (blue). Synthetic source (green dot) positioned at the transverse occipital sulcus.*

Since the source is set as distal as possible within the occipital lobe, the injected pattern is more likely to disperse towards the contralateral region of the head model. Due to the morphological structure of the white matter at this cortex, the model is able to concentrate vast amounts of energy from the source throughout the whole lobe (Fig. 6.14). This effect is clearly visible in this case compared against the other cases.

The linear programming solver can easily locate feasible results with relatively low termination tolerance and alpha values. Taking into account the scaled colors that are presented in Fig. 6.9, the minimal cost of the general results is obtained when both $TolFun = 1e^{-7}$ and $\alpha = 1e^{10}$, granting a result as minimal as $min\|\mathbf{y}_{(4,4)}\|_1 = 0.6832$ mA. After setting threshold limits, the required parameters to obtain minimum cost remain the same as the previously mentioned version. In the case when the threshold limit is set at 12.5%, the minimum cost value is $min\|\mathbf{y}_{(4,4,1)}\|_1 = 0.7151$ mA. In comparison with the somatosensory case, the residual values are high whenever the linear programming solver cannot find feasible solutions, attributed to the fact that the discretized primary current distribution is mainly concentrated within the boundaries of the region of interest.

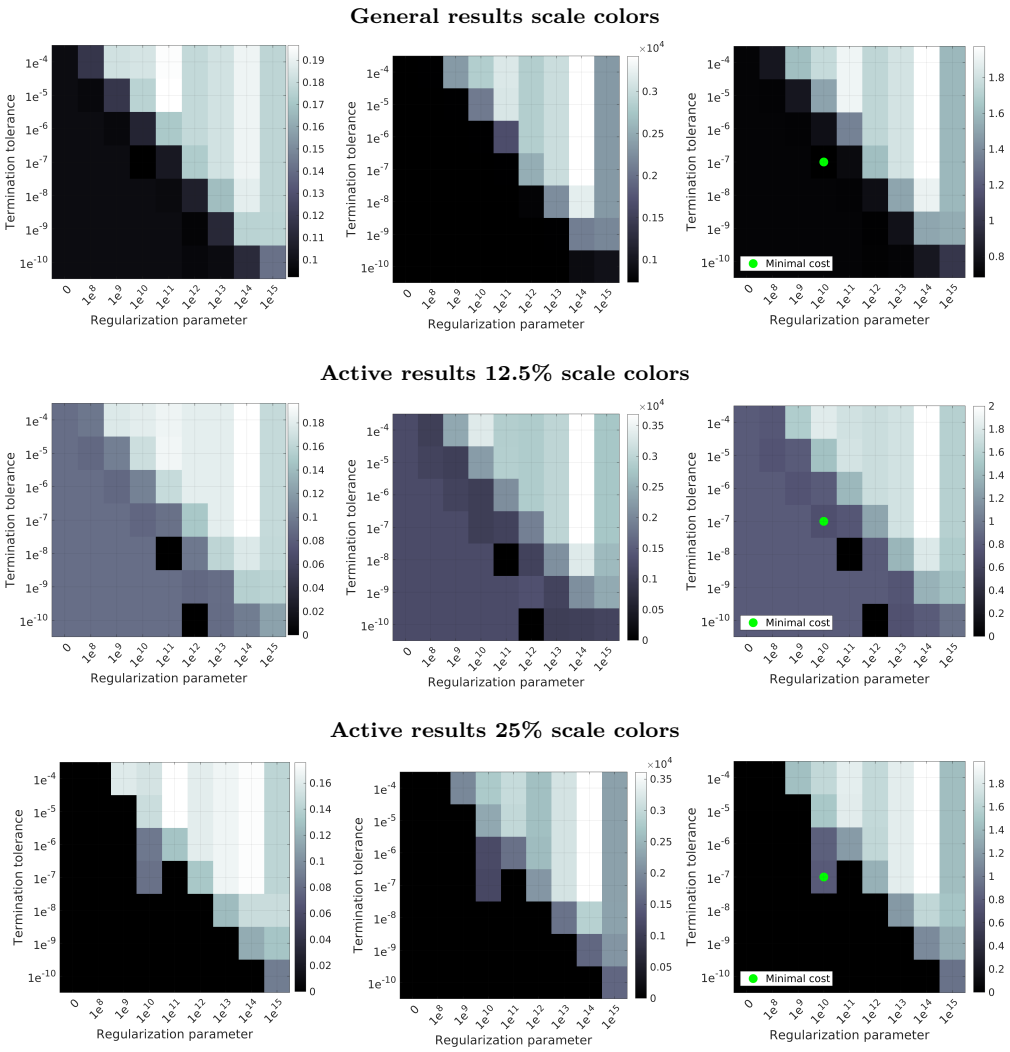

Figure 6.9 *scaled-color representations of the normalized results based on regularization parameter and termination tolerance.* ***Left:*** *Current values (y).* ***Middle:*** *Residual values.* ***Right:*** *Maximum absolute sum of current values and residuals. Minimal cost highlighted as a green dot.*

When the threshold limit is set at 25%, the model for finding feasible results became as strict as in the previous case. Interestingly, the solver was able to find feasibility using the same termination tolerance levels and alpha values. The minimum value obtained in these circumstances is $min\|\mathbf{y}_{(4,4,2)}\|_1 = 0.7905$ mA. Should the active results using the 4th n scalar column not be utilized, the next parameters required are the same values as the somatosensory case did (using $TolFun = 1e^{-8}$ and $\alpha = 1e^{14}$).

By comparing the results in Fig. 6.10, the normalized non-regularized and regularized current patterns with source located at the transverse occipital sulcus are much less sporadic and yield a better sparse distribution than the case with the source at the postcentral sulcus. Rather than inverting injected polarities, the non-

regularized version require some of the electrode channels to carry lower amperage values instead compared to their regularized version.

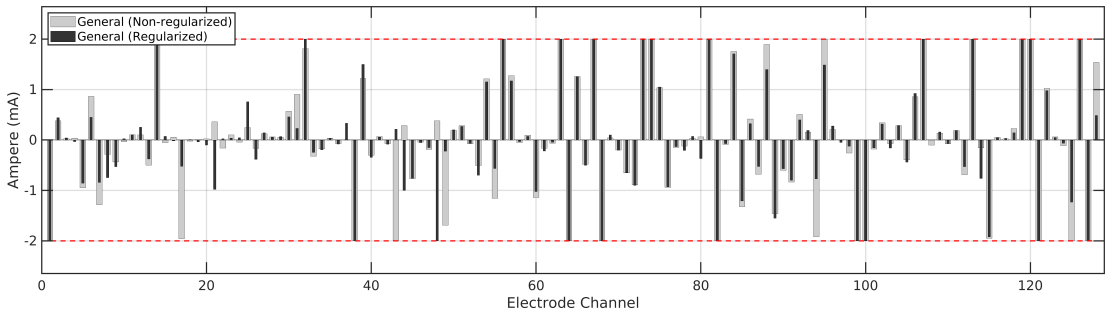

Figure 6.10 *Comparison of non-regularized and optimum regularized current pattern distribution across the 128 channels with synthetic source dipole at the transverse occipital sulcus.*

Using the above-mentioned minimal feasible solution, the threshold and active versions at 12.5% (Fig. 6.11) and 25% (Fig. 6.12) are presented. Straightaway, we can recognize that the total number of active electrode channels required to reproduce the electric field is dramatically reduced, compared to the general version. With the former threshold percentage, only 76 channels are required to be active. Moreover, using the latter threshold percentage, the potential distribution can be concentrated even further by reducing the available active channels down to 58 channels instead. The comparison between the general version and the reduced montage equivalents are displayed in Fig. 6.13.

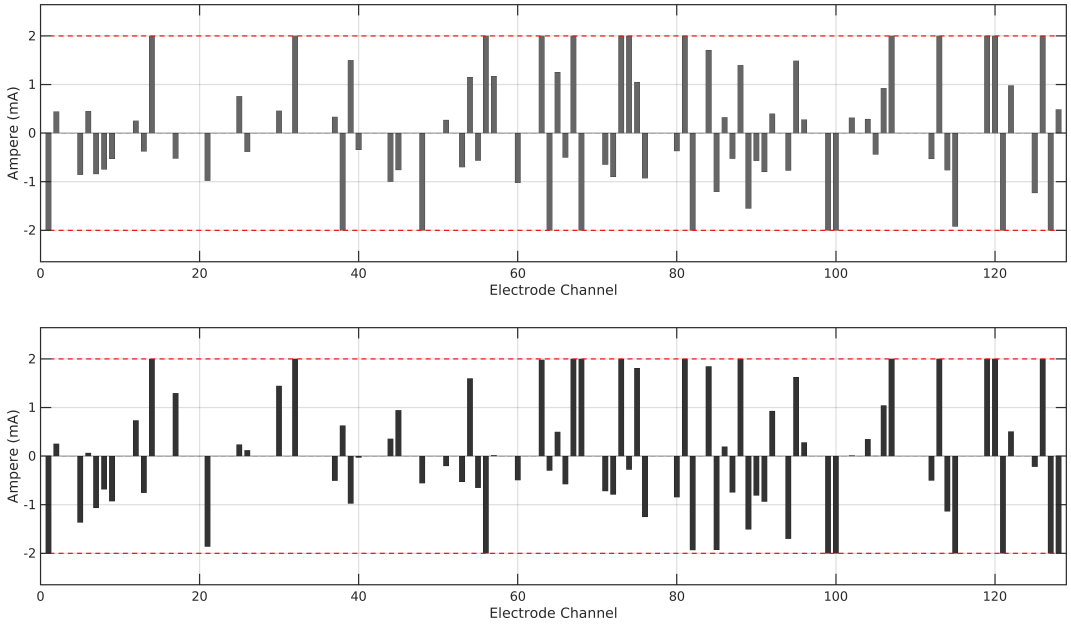

Figure 6.11 Top*: Thresholded current pattern distribution (12.5%).* ***Bot****: Active reduced montage current pattern distribution.*

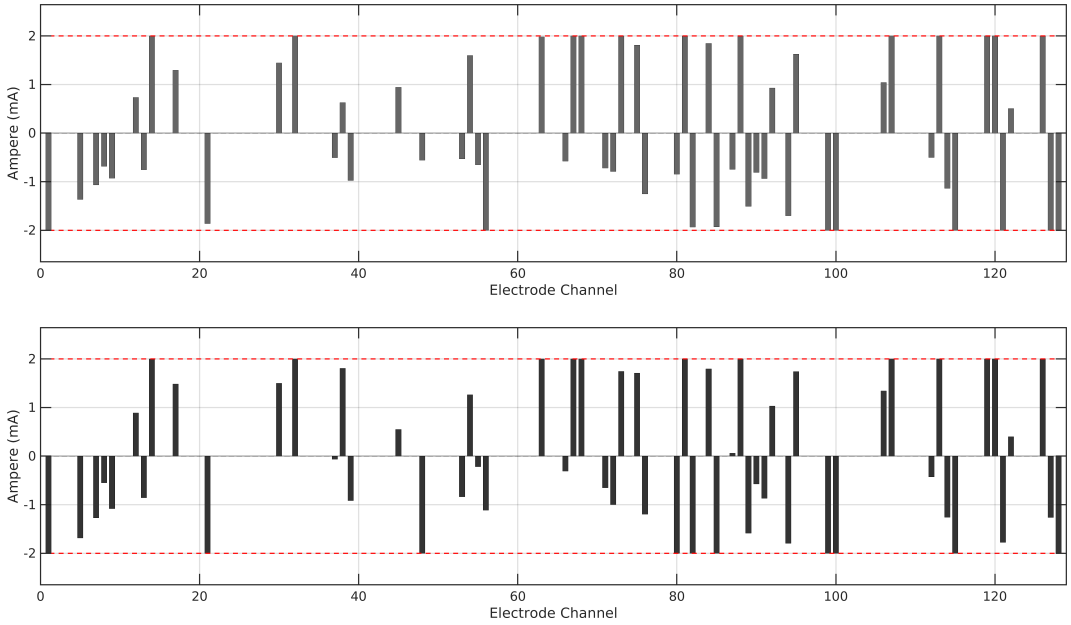

***Figure 6.12 Top**: Thresholded current pattern distribution (25%). **Bot**: Active reduced montage current pattern distribution.*

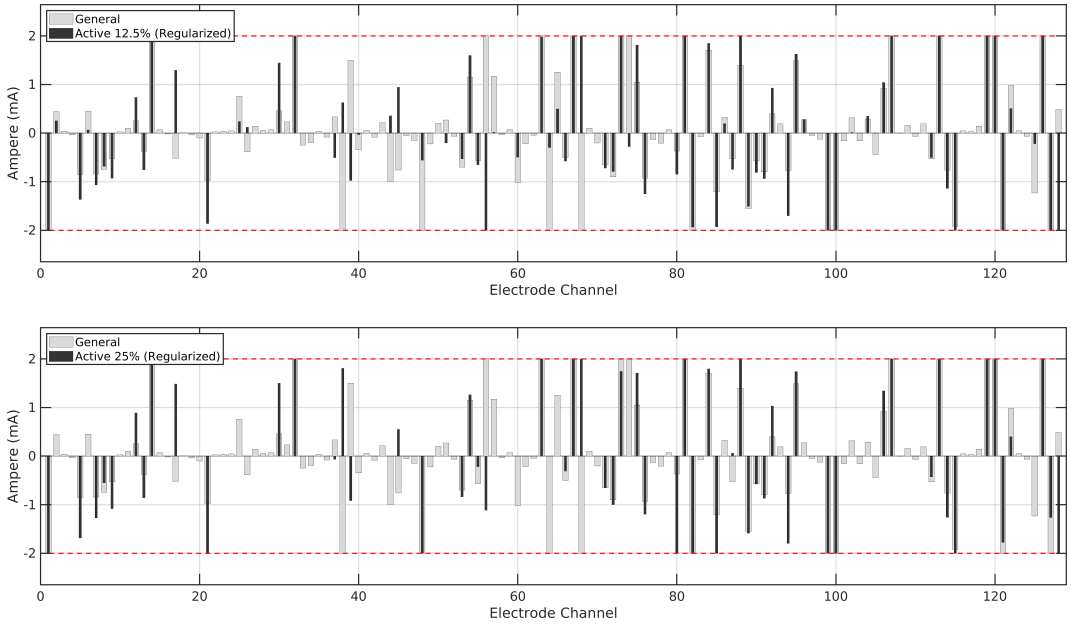

***Figure 6.13** Comparison of regularized and active current pattern with source located at transverse occipital sulcus. **Top:** General and reduced 12.5% version. **Bottom:** General and reduced 25% version.*

Based from the reconstructions and topographies (Fig. 6.14), different observations can be distinguished. First, based from the topographies, a reduced montage version has lower electrical concentrations. Second, the electric field of the 12.5%

version, even though uses more electrode channels than the 25% version, has a high-concentration at low-dispersion attributed to the increased levels of residual values obtained by the linear programming solver. Lastly, activity at the far-end of the occipital lobe of the right hemisphere increases as the number of electrode channels are reduced.

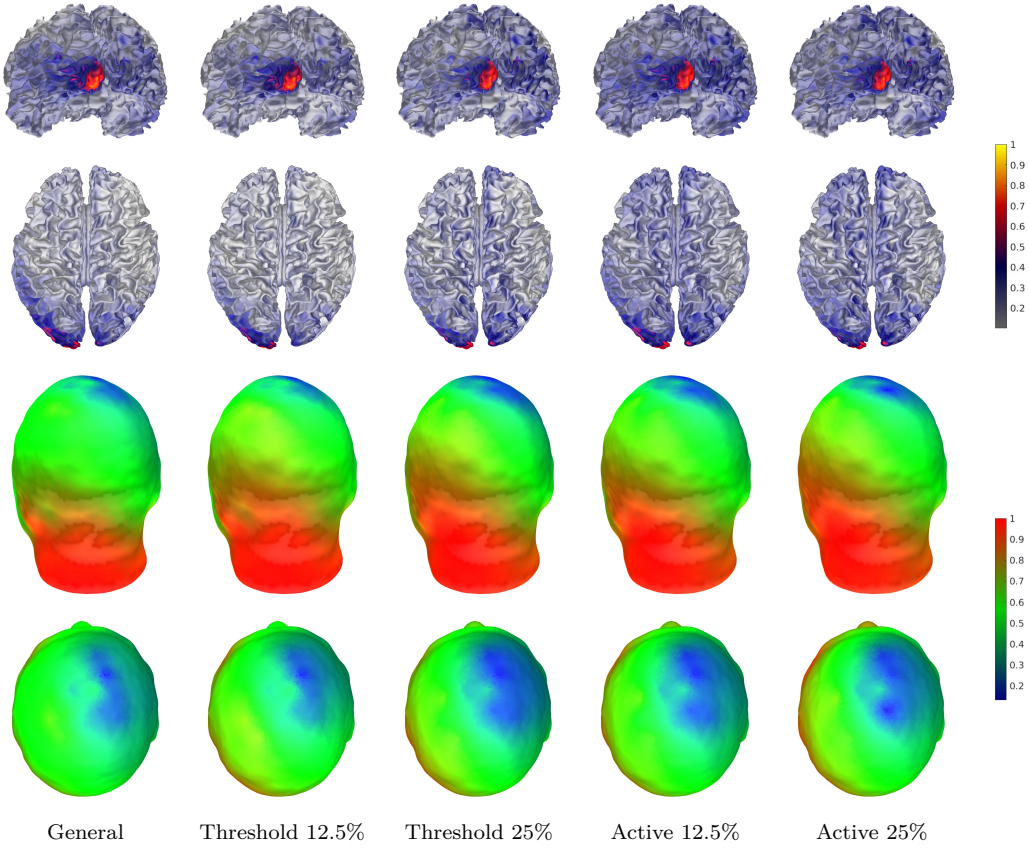

Figure 6.14 *Reconstructions and topographies using optimum tolerance and regularization with dipole simulated at the transverse occipital sulcus, left hemisphere.*

6.3 Case III - Auditory Cortex

We approach the temporal lobe and their surroundings. Similar to the previously cases we attach the source dipole (displayed with red color, to contrast against parcellation) nearby the superior temporal sulcus as in 6.15 using the coordinates (-60,-30,20) in ZI and with orientation (0,1,0) aiming in a rostral technique towards the rest of the sulcus. The behaviour of the electric field is expected to resemble, at some degree, part of the somatosensory results due to source proximities. In this case, is set as distal to cover as much as possible the perimeters of the temporal lobe, however, due to the proximities with the pariental lobe, there is a possibility that generated patterns reaches the boundaries of the latter lobe.

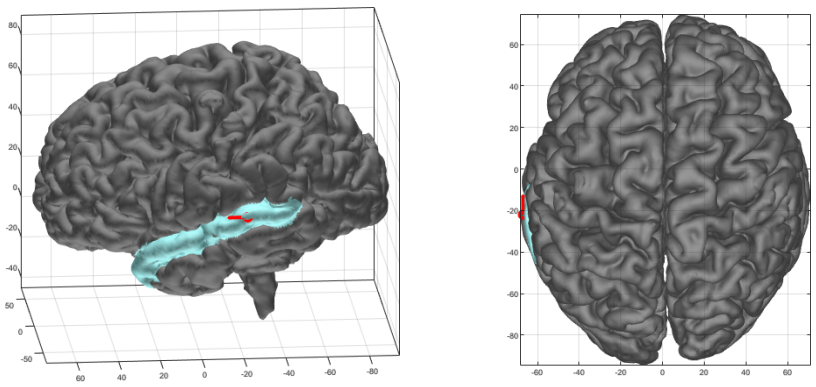

Figure 6.15 *Parcellation of left hemisphere temporal gyrus (cyan). Synthetic source (red dot) positioned at the superior temporal sulcus.*

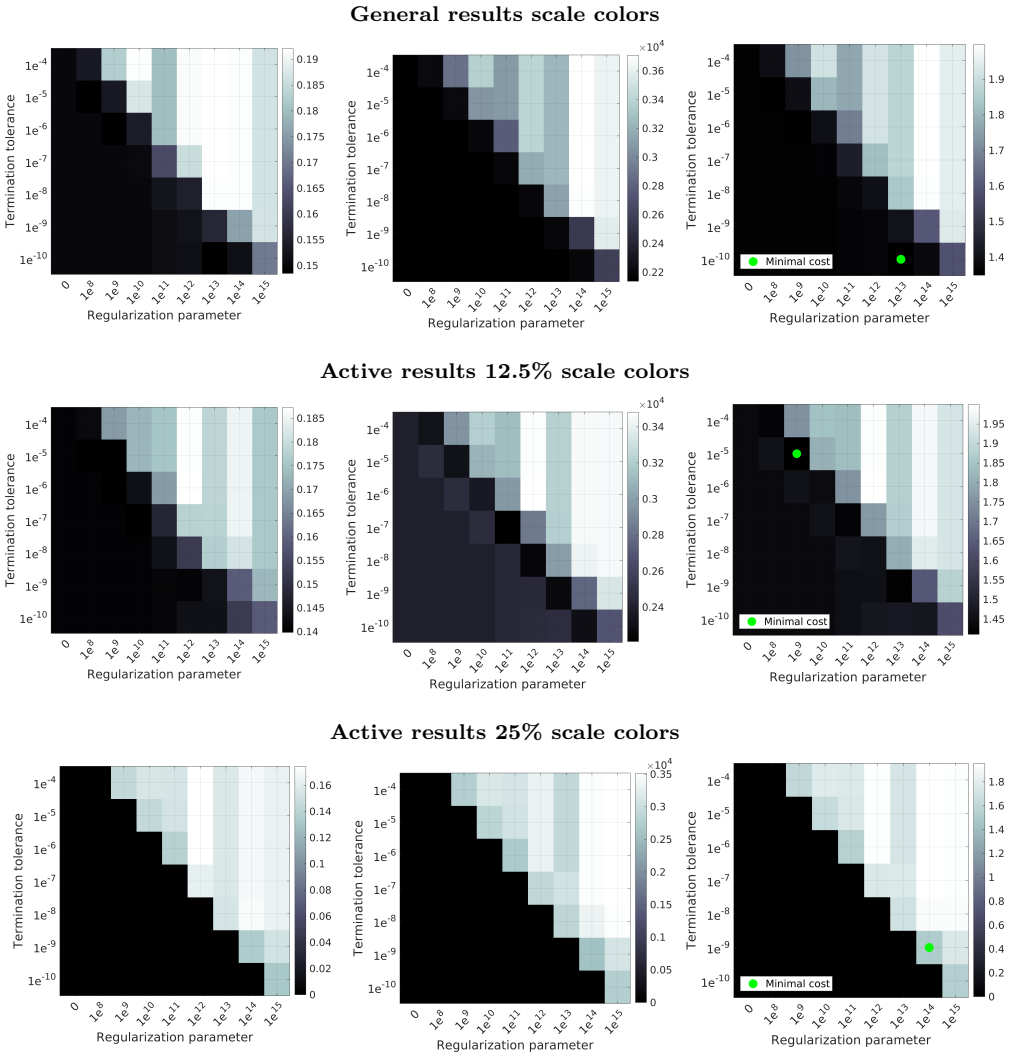

Figure 6.16 *scaled-color representations of the normalized results based on regularization parameter and termination tolerance.* ***Left:*** *Current values (y).* ***Middle:*** *Residual values.* ***Right:*** *Maximum absolute sum of current values and residuals. Minimal cost highlighted as a green dot.*

With the dipole set at the superior temporal sulcus, the tolerance/parametric results are plotted as in scaled-color image. Here, each cell represents the amount of total electric potential, residual values, and ℓ_1 norm from the current pattern. Additionally, the scaled-color values of threshold and active results using 12.5% and 25% are included and displayed in Fig. 6.16. Out of the total 63 cases on each situation and threshold value, the minimal potential is indicated (green dot) on the cell of ℓ_1 norm that yields the lowest value.

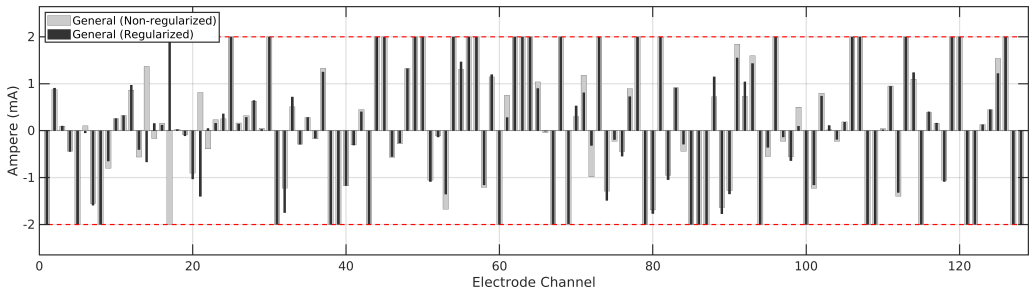

Figure 6.17 *Comparison of non-regularized and regularized current pattern distribution across the 128 channels with dipole at the superior temporal sulcus, left hemisphere.*

Evaluating the obtained results as scaled colors, to calculate the minimal cost without thresholding, the m scalar value is required to be set at the highest tolerance that the optimization toolbox can possible allow ($TolFun = 1e^{-10}$) and the n scalar value setting the regularization to $\alpha = 1e^{13}$. This regularization/tolerance values yields a total cost of $min\|\mathbf{y}_{(7,7)}\|_1 = 1.3491$ mA. Compared against the non-regularized version, $\alpha = 0$, the results obtained do not have much difference (Fig. 6.17). This is because the results obtained, despite considered to be mathematically feasible, are in fact unpractical and, rather, may cause detrimental effects if said parameters are to be used because the solution for this model has done *overfitting*. In statistics and machine-learning, overfitting is the term used when the task for data analysis holds close or resembles exactly a set of data that renders the classification unable to evaluate correctly new incoming data because of high variance levels (Hawkins 2004). In our case, the level of parameters required to be justified for this model are too many, this is because of high levels of α parameter that increases the weight in the data set, up to the point where noise, in the form of evaluation error, is now considered to take part as the correct result. To solve the issue, we re-evaluate with lesser electrodes as in the previous cases.

With the reduction of electrode channels, we can re-calculate a more practical model. With threshold value of 12.5%, we downsize the montage from 128 electrodes to use only 107 channels. The optimal tolerance/penalization terms are now set to be $TolFun = 1e^{-5}$ and $\alpha = 1e^{9}$. Using these terms, the minimal cost calculated is $min\|\mathbf{y}_{(2,3,1)}\|_1 = 1.4106$ mA (Fig. 6.18). For the case of threshold value of 25%,

the montage is further reduced to 97 channel version, the m and n scalar values are set for parameters $TolFun = 1e^{-9}$ and $\alpha = 1e^{14}$. The resulting minimal cost is $min\|\mathbf{y}_{(6,8,2)}\|_1 = 1.5043$ mA (Fig. 6.19).

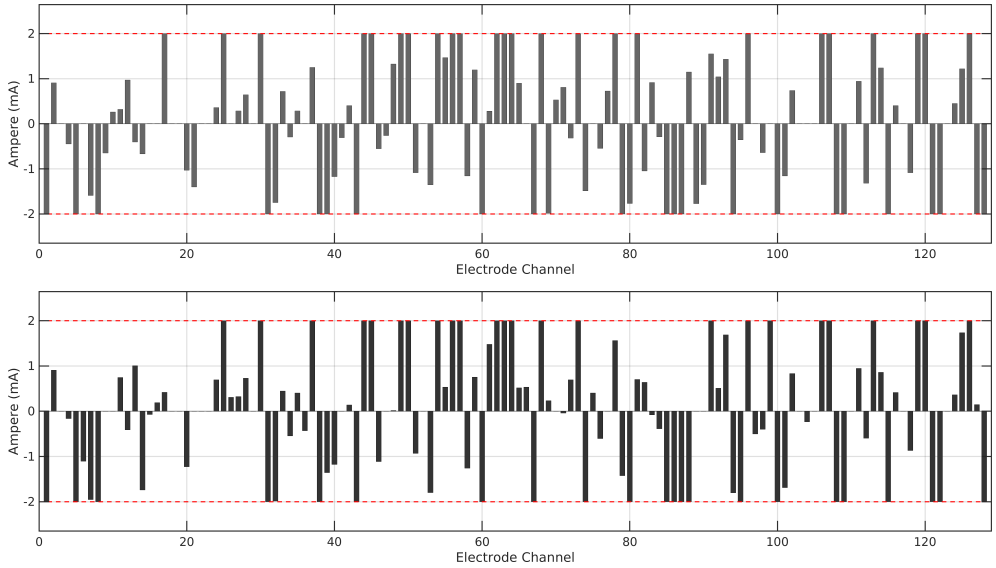

***Figure 6.18 Top**: Thresholded regularized current pattern distribution (12.5%). **Bot**: Active reduced montage current pattern distribution.*

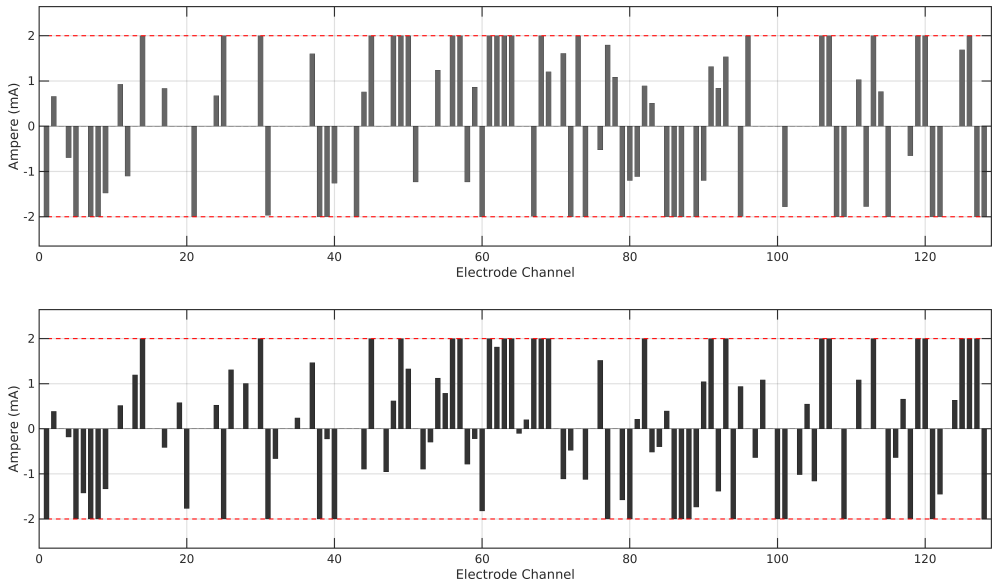

***Figure 6.19 Top**: Thresholded regularized current pattern distribution (25%). **Bot**: Active reduced montage current pattern distribution.*

Based on the results obtained, general and thresholds scenarios, share a strong resemble as in the somatosensory case. This can be justifiable due to the configuration similarities that were declared in ZI prior the calculations. The comparison

between the general version and the reduced montage using 12.5% and 25% are displayed in Fig. 6.20.

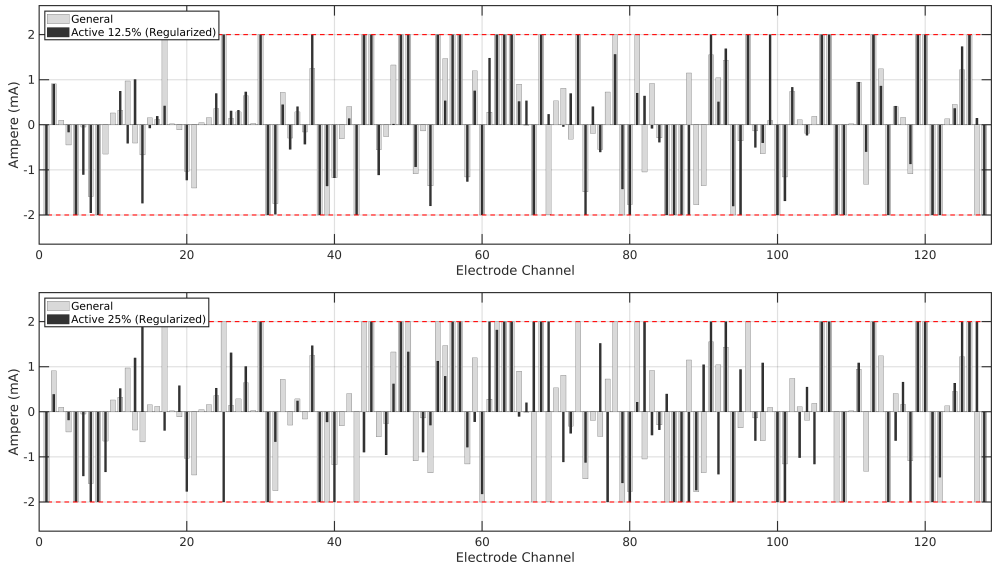

Figure 6.20 *Comparison of active current pattern distribution.* ***Top:*** *General regularized and reduced 12.5% version.* ***Bottom:*** *General regularized and reduced 25% version.*

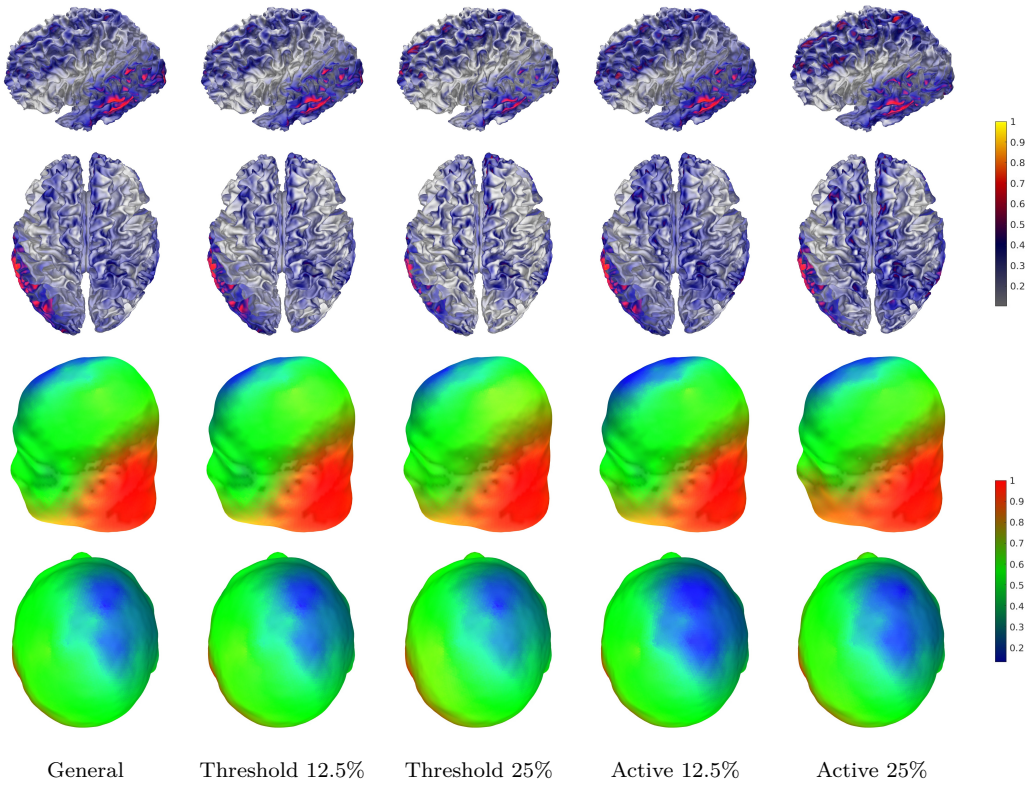

Figure 6.21 *Reconstructions and topographies using optimum tolerance and regularization with dipole simulated at the superior temporal sulcus, left hemisphere.*

7 Discussion

The present implementation covers both forward and inverse solver for MC-tES (Moreno-Duarte et al. 2014). The former one of these was built on the Zeffiro Interface's (ZI's) (He et al. 2019) existing EEG forward solver (Miinalainen et al. 2019) using the mathematical approach that couples the complete electrode model (CEM) boundary conditions (Pursiainen et al. 2018) with the governing differential equation of the electric field which follows from the point-wise Dirichlet current conservation condition for the total current density inside the head. The system that follows is an accurate description of the current flow in the different parts of the computing domain, including the complex-shaped brain and head models as well as the electrodes and their boundaries taking into account the exact contact surface area of the electrode. The forward model can be discretized using the finite element method (FEM) through the approach already utilized in ZI's EEG solver. Therefore, the implementation of the forward solver was a straightforward task and particularly well-suited for the ZI platform. The codes for constructing the matrices of the discretized MC-tES forward model, presented in this thesis, were already available in ZI. That is, the forward solver was obtained by re-organizing and re-developing the existing FEM solver components utilized by ZI. Consequently, it is obvious that, when implemented via the CEM, the EEG and MC-tES forward solvers are inherently connected, as they follow from a single mathematical model, that is also why it is essential from the mathematical point of view to have both implemented in a single computing platform. Due to their mathematical similarity, the processing times achieved with EEG and MC-tES forward solver are similar: a lead field matrix corresponding to a FEM discretization with a 1 mm resolution can be obtained within about 30 minutes with a contemporary workstation computer equipped with sufficiently large memory capacities and graphic processing unit (GPU). Here, the equipment used included DELL 5820[1]workstation with 128 Gigabytes of RAM (random access memory), Intel i9-10900X central processing unit (CPU) and Nvidia Quadro RTX 4000 GPU with 8 GB of RAM of its own.

The optimization-based inverse solver aims at minimizing, inside the brain, the support of the current density resulting from a MC-tES stimulus. In other words, it tries to maximize the set in which the current density vanishes. That is why the ℓ_1-norm minimization of the residual vector between a given current density within the brain and the volume current density due to the stimulus has been selected as the primary approach to seek the stimulus current pattern (Uutela et al. 1999). Namely, the ℓ_1-norm, i.e., the sum of the vector entry absolute values, is known to

[1] `https://en.wikipedia.org/wiki/Dell_Precision`, Dell Inc.

be small for vectors with only few non-zero entries. Furthermore, the ℓ_1-norm based regularization was applied to penalize the current pattern of the stimulus itself, as it needs to be as sparse as possible in order to minimize the current dose given to the subject, otherwise, non-regularized solutions, based on the solutions, would require the potential levels to inject high values of current in a singular channel. Safe MC-tES practicalities requires clinicians and researches to establish limit values both during and after a stimulation session to prevent harmful results to the subjects, or, if possible to avoid, adverse effects. That is why sparsity is of importance in this manner (Krishnaswamy et al. 2017). The optimization task following from this combined ℓ_1-norm optimization and penalization approach could be formulated as a linear programming task which, after a re-formulation presented in this thesis, was found to be directly implementable using MATLAB's already built-in linprog function. Of the solver algorithms, the dual-simplex method, i.e., dual problem solver, was found to perform well with the present optimization task. The obvious reason being the dimensionality of the lead field matrix which has considerably greater number of rows (degrees of freedom for the current density) than columns (the dimension of the stimulus current pattern). Consequently, the dual problem utilizing the transpose of the lead field matrix instead of the matrix itself, has considerably fewer constraints to be taken into account by the solver.

The regularization/tolerance combination to yield an optimal outcome with respect to the physiological parameters of the stimulation, e.g., the strength of the stimulus and the norm of the residual, was found to depend on the target area of the stimulus, that is why it is suggested that the optimization routine cannot rely on a fixed regularization/tolerance parameter but rather a set of systems are required to be calculated beforehand in order to ensure the appropriateness of the value pair applied. The present numerical experiments sketch rough working limits for the regularization parameter and tolerance value, using somatosensory, visual and auditory target areas as a reference. However, the present results should be verified with a more extensive study, including multiple subjects, in order to ensure their validity. Another research question to be investigated in the future is, whether an algorithm of finding the right regularization/tolerance combination can be developed in order to minimize the number of trials necessary in the optimization stage and, thereby, to speed up the computation. Here, a regular grid was used which might be a sub-optimal strategy regarding the computing time and effort, even though it can be interpreted to provide the most robust result.

The optimization problem was found to be solvable with physiologically applicable limits for the stimulus current: a synthetic 10 nAm source with a $40^{3/2} \approx 253$ mm^3 extent (Hari and Puce 2017) could be obtained with generally tolerable ± 2 mA (Nitsche 2003) as the limit for the maximal injected current amplitude. It was

found that, without regularization or thresholding, the current patterns obtained are likely to include only few close-to-zero values. The current dose given to the subject can be reduced both via increasing the threshold of minimal non-zero current or the value of the regularization parameter. In the former case 25%, i.e., approximately 0.5 mA, was found to be a critical range after which the optimizer might not find an appropriate solution anymore, when re-iterated (active case), and in the latter one, the residual norm was observed to diverge after a critical limit. Thus, it seems to be difficult to significantly reduce the current patterns obtained in this thesis, minimally with approximately 100 non-zero currents, without significantly compromising the focality of the volume current density in the brain.

A further reduction in the number of non-zero currents might be obtained by introducing a fixed pattern, similar to the 4x1 HD-tDCS method used in Caparelli-Daquer et al. 2012 and Borckardt et al. 2012. Such patterns were initially examined in this thesis, suggesting that the implemented optimizer algorithm is applicable as is also with those. A more extensive in examination can be conducted in the future, concentrating on the differences between the solvability of the optimization problem and the focality of the resulting current distribution in the brain.

8 Conclusion

This thesis described the mathematical methodology of transcranial electrical stimulation (MC-tES) and its computational implementation in the open Matlab-based Zeffiro Interface (ZI) toolbox with the principal goal to extend the applicability of ZI in different brain-related applications, and by using the solver implementation, among other things, to enlighten the process of finding an optimized current pattern and to provide codes for further development. The present implementation covers both forward and inverse MC-tES solver. The former one of these was built on the ZI's existing EEG forward solver and the latter utilizes an ℓ_1-regularized optimization approach. The solvers implemented were found to result in a feasible computing time when using a workstation with sufficient large memory and high-performance GPU unit. if intense amount of data is required to be rendered an if CPU or a lower performance GPU unit is used, ZI will be unable to render the data and causes the calculations to be interrupted.

Bibliography

Antal, A. et al. (2003). "Manipulation of phosphene thresholds by transcranial direct current stimulation in man". In: *Experimental Brain Research* 150.3, pp. 375–378. ISSN: 1432-1106. DOI: https://doi.org/10.1007/s00221-003-1459-8.

Antal, A. et al. (2008). "Comparatively weak after-effects of transcranial alternating current stimulation (tACS) on cortical excitability in humans". In: *Brain Stimulation* 1.2, pp. 97 –105. ISSN: 1935-861X. DOI: https://doi.org/10.1016/j.brs.2007.10.001. URL: http://www.sciencedirect.com/science/article/pii/S1935861X07000125.

Benninger, D. H. et al. (2010). "Transcranial direct current stimulation for the treatment of Parkinson's disease". In: *Journal of Neurology, Neurosurgery & Psychiatry* 81.10, pp. 1105–1111. ISSN: 0022-3050. DOI: https://doi.org/10.1136/jnnp.2009.202556.

Bikson, M. et al. (2004). "Effect of uniform extracellular DC electric fields on excitability in rat hippocampal slices in vitro". In: *Journal of Physiology* 557.1, pp. 175–190. DOI: https://10.1113/jphysiol.2003.055772.

Boggio, P. S. et al. (2006). "Effects of transcranial direct current stimulation on working memory in patients with Parkinson's disease". In: *Journal of the Neurological Sciences* 249.1. Terrorism for the Neurologist, pp. 31 –38. ISSN: 0022-510X. DOI: https://doi.org/10.1016/j.jns.2006.05.062.

Boggio, P. S. et al. (2007). "Go-no-go task performance improvement after anodal transcranial DC stimulation of the left dorsolateral prefrontal cortex in major depression". In: *Journal of Affective Disorders* 101.1, pp. 91 –98. ISSN: 0165-0327. DOI: https://doi.org/10.1016/j.jad.2006.10.026.

Boggio, P. S. et al. (2008). "Prefrontal cortex modulation using transcranial DC stimulation reduces alcohol craving: A double-blind, sham-controlled study". In: *Drug and Alcohol Dependence* 92.1, pp. 55 –60. ISSN: 0376-8716. DOI: https://doi.org/10.1016/j.drugalcdep.2007.06.011.

Borckardt, J. J. et al. (2012). "A Pilot Study of the Tolerability and Effects of High-Definition Transcranial Direct Current Stimulation (HD-tDCS) on Pain Perception". In: *The Journal of Pain* 13.2, pp. 112 –120. ISSN: 1526-5900. DOI: https://doi.org/10.1016/j.jpain.2011.07.001. URL: http://www.sciencedirect.com/science/article/pii/S1526590011006651.

Boyd, S. and L. Vandenberghe (2004). *Convex Optimization*. Cambridge University Press. ISBN: 9781107394001. URL: https://books.google.fi/books?id=IUZdAAAAQBAJ.

Brau, C. (2003). *Modern Problems in Classical Electrodynamics*. OUP USA. ISBN: 9780195146653. URL: https://books.google.fi/books?id=mUrawAEACAAJ.

Brodmann, K. (2007). *Brodmann's: Localisation in the cerebral cortex*. Springer Science & Business Media.

Caparelli-Daquer, E. M. et al. (2012). "A pilot study on effects of 4×1 High-Definition tDCS on motor cortex excitability". In: *2012 Annual International Conference of the IEEE Engineering in Medicine and Biology Society*, pp. 735–738. DOI: 10.1109/EMBC.2012.6346036.

Chaieb, L., W. Paulus, and A. Antal (2011). "Evaluating aftereffects of short-duration transcranial random noise stimulation on cortical excitability". In: *Neural plasticity* 2011.

Dannhauer, M et al. (2011). "Modeling of the human skull in EEG source analysis". In: *Human Brain Mapping* 32, pp. 1383–1399. DOI: 10.1002/hbm.21114.

DaSilva, A. F. et al. (2011). "Electrode Positioning and Montage in Transcranial Direct Current Stimulation". In: *JoVE* 51, e2744. ISSN: 1940-087X. DOI: https://doi.org/10.3791/2744.

Datta, A. et al. (2009). "Gyri-precise head model of transcranial direct current stimulation: Improved spatial focality using a ring electrode versus conventional rectangular pad". In: 2.4, 201–207.e1. DOI: https://doi.org/10.1016/j.brs.2009.03.005.

Datta, A. et al. (2011). "Individualized model predicts brain current flow during transcranial direct-current stimulation treatment in responsive stroke patient". In: *Brain Stimulation* 4.3, pp. 169 –174. ISSN: 1935-861X. DOI: https://doi.org/10.1016/j.brs.2010.11.001.

Datta, A. et al. (2013). "Cranial electrotherapy stimulation and transcranial pulsed current stimulation: a computer based high-resolution modeling study". In: *Neuroimage* 65, pp. 280–287.

Francis, J. T., B. J. Gluckman, and S. J. Schiff (2003). "Sensitivity of Neurons to Weak Electric Fields". In: *Journal of Neuroscience* 23.19, pp. 7255–7261. ISSN: 0270-6474. DOI: 10.1523/JNEUROSCI.23-19-07255.2003. eprint: https://www.jneurosci.org/content/23/19/7255.full.pdf. URL: https://www.jneurosci.org/content/23/19/7255.

Fregni, F et al. (2005a). "Non-invasive brain stimulation for Parkinson's disease: a systematic review and meta-analysis of the literature". In: *Journal of Neurology, Neurosurgery & Psychiatry* 76.12, pp. 1614–1623. ISSN: 0022-3050. DOI: https://doi.org/10.1136/jnnp.2005.069849.

Fregni, F. et al. (2005b). "Transcranial direct current stimulation". In: *British Journal of Psychiatry* 186.5, pp. 446–447. DOI: https://doi.org/10.1192/bjp.186.5.446.

Fregni, F. et al. (2005c). "Anodal transcranial direct current stimulation of prefrontal cortex enhances working memory". In: *Experimental Brain Research* 166.1, pp. 23–30. ISSN: 1432-1106. DOI: https://doi.org/10.1007/s00221-005-2334-6.

Fregni, F. et al. (2006a). "A Controlled Clinical Trial of Cathodal DC Polarization in Patients with Refractory Epilepsy". In: *Epilepsia* 47.2, pp. 335–342. DOI: https://doi.org/10.1111/j.1528-1167.2006.00426.x.

Fregni, F. et al. (2006b). "A randomized, sham-controlled, proof of principle study of transcranial direct current stimulation for the treatment of pain in fibromyalgia". In: *Arthritis & Rheumatism* 54.12, pp. 3988–3998. DOI: https://doi.org/10.1002/art.22195.

Fregni, F. et al. (2006c). "Noninvasive cortical stimulation with transcranial direct current stimulation in Parkinson's disease". In: *Movement Disorders* 21.10, pp. 1693–1702. DOI: https://doi.org/10.1002/mds.21012.

Fregni, F. et al. (2006d). "Treatment of major depression with transcranial direct current stimulation." In: *Bipolar Disorders* 8.2, pp. 203–204. DOI: https://doi.org/10.1111/j.1399-5618.2006.00291.x.

Furubayashi, T. et al. (2008). "Short and long duration transcranial direct current stimulation (tDCS) over the human hand motor area". In: *Experimental Brain Research* 185.2, pp. 279–286. ISSN: 1432-1106. DOI: https://doi.org/10.1007/s00221-007-1149-z.

Guleyupoglu, B. et al. (2013). "Classification of methods in transcranial Electrical Stimulation (tES) and evolving strategy from historical approaches to contemporary innovations". In: *Journal of Neuroscience Methods* 219.2, pp. 297 – 311. ISSN: 0165-0270. DOI: https://doi.org/10.1016/j.jneumeth.2013.07.016. URL: http://www.sciencedirect.com/science/article/pii/S0165027013002549.

Hanke, M., B. Harrach, and N. Hyvönen (June 2011). "Justification of point electrode models in electrical impedance tomography". In: *Mathematical Models and Methods in Applied Sciences* 21. DOI: 10.1142/S0218202511005362.

Hari, R. and A. Puce (2017). *MEG-EEG Primer*. Oxford University Press.

Hawkins, D. M. (2004). "The Problem of Overfitting". In: *Journal of Chemical Information and Computer Sciences* 44.1, pp. 1–12. DOI: 10.1021/ci0342472. URL: https://doi.org/10.1021/ci0342472.

He, Q., A. Rezaei, and S. Pursiainen (2019). "Zeffiro User Interface for Electromagnetic Brain Imaging: a GPU Accelerated FEM Tool for Forward and Inverse Computations in Matlab". English. In: *Neuroinformatics*. ISSN: 1539-2791. DOI: 10.1007/s12021-019-09436-9.

Hämäläinen, M. et al. (1993). "Magnetoencephalography: Theory, instrumentation, and applications to noninvasive studies of the working human brain". In: *Rev. Mod. Phys.* 65, pp. 413–. DOI: 10.1103/RevModPhys.65.413.

Jäkel, S. and L. Dimou (2017). "Glial Cells and Their Function in the Adult Brain: A Journey through the History of Their Ablation". In: *Frontiers in Cellular Neuroscience* 11, p. 24. ISSN: 1662-5102. DOI: 10.3389/fncel.2017.00024. URL: https://www.frontiersin.org/article/10.3389/fncel.2017.00024.

Kaipio, J. and E. Somersalo (2006). *Statistical and computational inverse problems*. Vol. 160. Springer Science & Business Media.

Kandel, E. et al. (2012). *Principles of Neural Science, Fifth Edition*. McGraw-Hill Education. ISBN: 9780071810012. URL: https://books.google.fi/books?id=Z2yVUTnlIQsC.

Kincses, T. Z. et al. (2004). "Facilitation of probabilistic classification learning by transcranial direct current stimulation of the prefrontal cortex in the human". In: *Neuropsychologia* 42.1, pp. 113–117.

Klem, G. H. (1999). "The ten-twenty electrode system of the international federation. the internanional federation of clinical nenrophysiology". In: *Electroencephalogr. Clin. Neurophysiol. Suppl.* 52, pp. 3–6.

Krishnaswamy, P. et al. (2017). "Sparsity enables estimation of both subcortical and cortical activity from MEG and EEG". In: *Proceedings of the National Academy of Sciences* 114.48, E10465–E10474.

Lindenberg, R. et al. (2010). "Bihemispheric brain stimulation facilitates motor recovery in chronic stroke patients". In: *Neurology* 75.24, pp. 2176–2184. ISSN: 0028-3878. DOI: https://doi.org/10.1212/WNL.0b013e318202013a.

Malmivuo, J., V. Suihko, and H. Eskola (Apr. 1997). "Sensitivity Distributions of EEG and MEG Measurements". In: *IEEE Transactions on Biomedical Engineering* 44, pp. 196–208. DOI: 10.1109/10.554766.

Miinalainen, T. et al. (2019). "A realistic, accurate and fast source modeling approach for the EEG forward problem". In: *NeuroImage* 184, pp. 56–67.

Miniussi, C., J. A. Harris, and M. Ruzzoli (2013). "Modelling non-invasive brain stimulation in cognitive neuroscience". In: *Neuroscience & Biobehavioral Reviews* 37.8, pp. 1702 –1712. ISSN: 0149-7634. DOI: https://doi.org/10.1016/j.neubiorev.2013.06.014. URL: http://www.sciencedirect.com/science/article/pii/S0149763413001693.

Montes-Restrepo, V. et al. (Jan. 2014). "Influence of Skull Modeling Approaches on EEG Source Localization". In: *Brain topography* 27, pp. 95–111. DOI: 10.1007/s10548-013-0313-y.

Moreno-Duarte, I. et al. (2014). "Chapter 2 - Transcranial Electrical Stimulation: Transcranial Direct Current Stimulation (tDCS), Transcranial Alternating Cur-

rent Stimulation (tACS), Transcranial Pulsed Current Stimulation (tPCS), and Transcranial Random Noise Stimulation (tRNS)". In: *The Stimulated Brain*. Ed. by R. Cohen Kadosh. San Diego: Academic Press, pp. 35 –59. ISBN: 978-0-12-404704-4. DOI: https://doi.org/10.1016/B978-0-12-404704-4.00002-8. URL: http://www.sciencedirect.com/science/article/pii/B9780124047044000028.

Nitsche, M. A. and W. Paulus (2000). "Excitability changes induced in the human motor cortex by weak transcranial direct current stimulation". In: *The Journal of Physiology* 527.3, pp. 633–639. DOI: https://doi.org/10.1111/j.1469-7793.2000.t01-1-00633.x.

Nitsche, M. A. (2003). "Safety criteria for transcranial direct current stimulation (tDCS) in humans". In: *Clin Neurophysiol* 114, pp. 2220–2222.

Nitsche, M. A. et al. (2003). "Facilitation of implicit motor learning by weak transcranial direct current stimulation of the primary motor cortex in the human". In: *Journal of cognitive neuroscience* 15.4, pp. 619–626.

Nitsche, M. A. et al. (2009). "Treatment of depression with transcranial direct current stimulation (tDCS): A Review". In: *Experimental Neurology* 219.1. Brain Stimulation in Psychiatry, pp. 14 –19. ISSN: 0014-4886. DOI: https://doi.org/10.1016/j.expneurol.2009.03.038.

Nunez, P. et al. (2006). *Electric Fields of the Brain: The Neurophysics of EEG*. Oxford University Press. ISBN: 9780195050387. URL: https://books.google.fi/books?id=fUv54as56_8C.

Paulus, W. (2011). "Transcranial electrical stimulation (tES – tDCS; tRNS, tACS) methods". In: *Neuropsychological Rehabilitation* 21.5, pp. 602–617. DOI: https://doi.org/10.1080/09602011.2011.557292.

Peterchev, A. V. et al. (2012). "Fundamentals of transcranial electric and magnetic stimulation dose: Definition, selection, and reporting practices". In: *Brain Stimulation* 5.4, pp. 435 –453. ISSN: 1935-861X. DOI: https://doi.org/10.1016/j.brs.2011.10.001. URL: http://www.sciencedirect.com/science/article/pii/S1935861X11001495.

Pursiainen, S, J Vorwerk, and C. H. Wolters (2016). "Electroencephalography (EEG) forward modeling viaH(div) finite element sources with focal interpolation". In: *Physics in Medicine and Biology* 61.24, pp. 8502–8520. DOI: 10.1088/0031-9155/61/24/8502. URL: https://doi.org/10.1088\%2F0031-9155\%2F61%2F24%2F8502.

Pursiainen, S. et al. (2018). "Advanced Boundary Electrode Modeling for tES and Parallel tES/EEG". In: *IEEE Transactions on Neural Systems and Rehabilitation Engineering* 26.1, pp. 37–44. DOI: 10.1109/TNSRE.2017.2748930.

Pursiainen, S., F. Lucka, and C. Wolters (Feb. 2012). "Complete electrode model in EEG: Relationship and differences to the point electrode model". In: *Physics in medicine and biology* 57, pp. 999–1017. DOI: https://doi.org/10.1088/0031-9155/57/4/999.

Rampersad, S, D Stegeman, and T Oostendorp (2013). "OP 11. optimized tDCS electrode configurations for five targets determined via an inverse FE modeling approach". In: *Clinical Neurophysiology* 124.10, e61–e62.

Robinovitch, L. G. (1914). "Electric Analgesia, and Electric Resuscitation After Heart Failure Under Chloroform or Electrocution". In: *Anesthesia. New York: Appleton*.

Rullmann, M. et al. (2009). "EEG source analysis of epileptiform activity using a 1 mm anisotropic hexahedra finite element head model". In: *NeuroImage* 44.2, pp. 399–410.

Sadiku, M. and P. Sadiku (2001). *Elements of Electromagnetics*. Oxford series in electrical and computer engineering. Oxford University Press. ISBN: 9780195134773. URL: https://books.google.fi/books?id=w2ITHQAACAAJ.

Schomer, D. and F. Lopes da Silva (Oct. 2012). *Niedermeyer's electroencephalography: Basic principles, clinical applications, and related fields: Sixth edition*, pp. 1–1269.

Somersalo, E., M. Cheney, and D. Isaacson (Aug. 1992). "Existence and Uniqueness for Electrode Models for Electric Current Computed Tomography". In: *SIAM J. Appl. Math.* 52.4, pp. 1023–1040. ISSN: 0036-1399. DOI: 10.1137/0152060. URL: https://doi.org/10.1137/0152060.

Song, M., Y. Shin, and K. Yun (2014). "Beta-frequency EEG activity increased during transcranial direct current stimulation". In: *NeuroReport* 25.18. ISSN: 0959-4965. DOI: 10.1097/WNR.0000000000000283.

Sörnmo, L. and P. Laguna (2005). *Bioelectrical Signal Processing in Cardiac and Neurological Applications*. Academic Press series in biomedical engineering. Elsevier Science. ISBN: 9780124375529. URL: https://books.google.fi/books?id=RQv7tFFXYyIC.

Tanzer, I. (2006). "Numerical modeling in electro- and magnetoencephalography". In:

Terney, D. et al. (2008). "Increasing Human Brain Excitability by Transcranial High-Frequency Random Noise Stimulation". In: *Journal of Neuroscience* 28.52, pp. 14147–14155. ISSN: 0270-6474. DOI: 10.1523/JNEUROSCI.4248-08.2008. eprint: https://www.jneurosci.org/content/28/52/14147.full.pdf. URL: https://www.jneurosci.org/content/28/52/14147.

Thut, G., P. Schyns, and J. Gross (2011). "Entrainment of Perceptually Relevant Brain Oscillations by Non-Invasive Rhythmic Stimulation of the Human Brain".

In: *Frontiers in Psychology* 2, p. 170. ISSN: 1664-1078. DOI: https://doi.org/10.3389/fpsyg.2011.00170.

Ukueberuwa, D. and E. M. Wassermann (2010). "Direct current brain polarization: a simple, noninvasive technique for human neuromodulation". In: *Neuromodulation : journal of the International Neuromodulation Society* 13.3, pp. 168–173. ISSN: 1525-1403. DOI: https://doi.org/10.1111/j.1525-1403.2010.00283.x.

Uutela, K., M Hämäläinen, and E. Somersalo (1999). "Visualization of magnetoencephalographic data using minimum current estimates". In: *NeuroImage* 10.2, pp. 173–180.

Vöröslakos, M. et al. (2018). "Direct effects of transcranial electric stimulation on brain circuits in rats and humans". In: *Nature Communications* 9.1, p. 483. ISSN: 2041-1723. DOI: https://doi.org/10.1038/s41467-018-02928-3.

Zaghi, S. et al. (2010). "Noninvasive Brain Stimulation with Low-Intensity Electrical Currents: Putative Mechanisms of Action for Direct and Alternating Current Stimulation". In: *The Neuroscientist* 16.3, pp. 285–307. DOI: https://doi.org/10.1177/1073858409336227.

A Optimization Script

Program A.1 *Zeffiro Interface (ZI) optimization fuction code for solving linear programming problem.*

```
function [y_tes, residual, flag_val] = ...
zef_optimize_tes_current(L_tes_projection, x_tes, varargin)
opts = optimset('linprog');

if length(varargin) >= 1
    param_struct = varargin{1};
else
    param_struct = [];
end
if isfield(param_struct,'active_electrodes')
    if  not(isempty(param_struct.active_electrodes))
        active_electrodes = param_struct.active_electrodes;
    else
        active_electrodes = [1:size(L_tes_projection,2)];
    end
else
    active_electrodes = [1:size(L_tes_projection,2)];
end
if isfield(param_struct,'positivity_constraint')
    if  not(isempty(param_struct.positivity_constraint))
        positivity_constraint = ...
        param_struct.positivity_constraint;
    end
    else
        positivity_constraint = [];
end
if isfield(param_struct,'negativity_constraint')
    if  not(isempty(param_struct.negativity_constraint))
        negativity_constraint = ...
        param_struct.negativity_constraint;
    end
    else
        negativity_constraint = [];
end
if isfield(param_struct,'max_amplitude')
    lower_bound = -(param_struct.max_amplitude);
```

```
    upper_bound =   param_struct.max_amplitude;
else
    lower_bound = -Inf;
    upper_bound =  Inf;
end
if isfield(param_struct,'reg_param')
    reg_param = param_struct.reg_param;
else
    reg_param = [];
end
if isfield(param_struct,'tolerance')
    opts.TolFun = param_struct.tolerance;
end
if isfield(param_struct,'constraint_tolerance')
    opts.TolCon = param_struct.constraint_tolerance;
end
if isfield(param_struct,'variable_tolerance')
    opts.TolX = param_struct.variable_tolerance;
end
if isfield(param_struct,'algorithm')
    opts.Algorithm = param_struct.algorithm;
end
if not(isempty(positivity_constraint))
p_c_ind = sub2ind([length(positivity_constraint) ...
size(L_tes_projection,2)], ...
[1:length(positivity_constraint)]', ...
positivity_constraint(:));
p_c_aux = zeros(length(positivity_constraint), ...
size(L_tes_projection,2));
p_c_aux(p_c_ind) = -1;
L_tes_projection = [L_tes_projection; p_c_aux];
x_tes = [x_tes ; zeros(length(positivity_constraint),1)];
end
if not(isempty(negativity_constraint))
n_c_ind = sub2ind([length(negativity_constraint) ...
size(L_tes_projection,2)],...
[1:length(negativity_constraint)]', ...
negativity_constraint(:));
n_c_aux = zeros(length(negativity_constraint), ...
size(L_tes_projection,2));
n_c_aux(n_c_ind) = 1;
L_tes_projection = [L_tes_projection; n_c_aux];
```

```
x_tes = [x_tes ; zeros(length(negativity_constraint),1)];
end

L_tes_projection = L_tes_projection(:,active_electrodes);

if length(lower_bound) <= 1
    lower_bound = ...
    lower_bound*ones(size(L_tes_projection,2),1);
end
if length(upper_bound) <= 1
    upper_bound = ...
    upper_bound*ones(size(L_tes_projection,2),1);
end

if isempty(reg_param)
    [y_tes,~,flag_val] = ...
    linprog(sum(L_tes_projection)', ...
    -L_tes_projection, ...
    -x_tes, ...
    ones(1,size(L_tes_projection,2)), ...
    0, lower_bound, upper_bound, opts);
else
    L_tes_projection = [L_tes_projection ; ...
    reg_param*ones(1,size(L_tes_projection,2))];
    x_tes = [x_tes; 0];

    [y_tes,~,flag_val] = ...
    linprog(sum(L_tes_projection)' ...
    +reg_param,...
    -L_tes_projection, ...
    -x_tes, ...
    ones(1,size(L_tes_projection,2)), ...
    0, lower_bound, upper_bound, opts);
end
if ismember(flag_val,[1 3])
    residual = norm(L_tes_projection*y_tes-x_tes,1);
else
    residual = 0;
end

end
```